SAN FRANCISCO ESTUARY & WATERSHED SCIENCE
Sponsored by the Delta Science Program and the UC Davis Muir Institute

RESEARCH

Dispersion and Stratification Dynamics in the Upper Sacramento River Deep Water Ship Channel

Leah E. K. Lenoch*[1], Paul R. Stumpner[1], Jon R. Burau[1], Luke C. Loken[2,3], Steve Sadro[3]

ABSTRACT

Hydrodynamics control the movement of water and material within and among habitats, where time-scales of mixing can exert bottom-up regulatory effects on aquatic ecosystems through their influence on primary production. The San Francisco Estuary (estuary) is a low-productivity ecosystem, which is in part responsible for constraining higher trophic levels, including fishes. Many research and habitat-restoration efforts trying to increase primary production have been conducted, including, as described here, a whole-ecosystem nutrient addition experiment where calcium nitrate was applied in the Sacramento River Deep Water Ship Channel (DWSC) to see if phytoplankton production could be increased and exported out of the DWSC. As an integral part of this experiment, we investigated the physical mechanisms that control mixing, and how these mechanisms affect the strength and duration of thermal stratification, which we revealed as critical for controlling phytoplankton dynamics in the relatively turbid upper DWSC. Analysis of a suite of mixing mechanisms and time-scales show that both tidal currents and wind control mixing rates and stratification dynamics in the DWSC. Longitudinal and vertical dispersion increased during periods of high wind, during which wind speed influenced dispersion more than tidal currents. Thermal stratification developed most days, which slowed vertical mixing but was rapidly broken down by wind-induced mixing. Stratification rarely persisted for longer than 24 hours, limiting phytoplankton production in the study area. The interaction between physical mechanisms that control mixing rates, mediate stratification dynamics, and ultimately limit primary production in the DWSC may be useful in informing habitat restoration elsewhere in the Delta and in other turbid aquatic environments.

KEY WORDS

Sacramento River Deep Water Ship Channel, hydrodynamics, dispersion, stratification

SFEWS Volume 19 | Issue 4 | Article 5

https://doi.org/10.15447/sfews.2021v19iss4art5

* Corresponding author: llenoch@usgs.gov

1 California Water Science Center
US Geological Survey
West Sacramento, CA 95819 USA

2 Upper Midwest Water Science Center
US Geological Survey
Middleton, WI 53562 USA

3 Department of Environmental Science and Policy
University of California, Davis
Davis, CA 95616 USA

INTRODUCTION

Hydrodynamics dictate the movement of water and material within and among all aquatic ecosystems. At the nexus of tidal influence and freshwater inflow, estuaries are complex systems that can maintain a high degree of complex channel morphology that drives habitat heterogeneity, contributing to spatiotemporal variability in habitat connectivity, transport, and mixing rates. Rates of mixing and transport in estuaries also vary with tidal current magnitude, wind, net advection, density stratification, and residual currents (Fischer et al. 1979). Tidal processes generally dominate horizontal dispersion, but dispersion rates can change based on a number of factors, including spring-neap cycle variability in tidal current strength (Fischer et al. 1979), incomplete vertical or lateral mixing (Geyer et al. 2008), and the interaction between tidal processes and channel morphology (Stumpner et al. 2020). Stratification can greatly reduce vertical mixing rates and, depending on the strength of stratification and time-scales of vertical mixing, can enhance horizontal transport through gravitational circulation in brackish water systems (Monismith et al. 1996) or increase horizontal dispersion rates as a result of increased vertical shear in systems without a horizontal density gradient (Geyer et al. 2008).

Time-scales of mixing can also exert a strong bottom-up regulatory effect on aquatic ecosystem functions. For example, mixing time-scales regulate exposure to both bottom-up (i.e., nutrients and light) and top-down (i.e., exposure to benthic filter feeders) factors that affect ecosystem metabolic rates and primary production (Cloern et al. 2014). The Sacramento–San Joaquin Delta (Delta) in the San Francisco Estuary (estuary) (Figure 1) is a low-productivity yet nutrient-rich

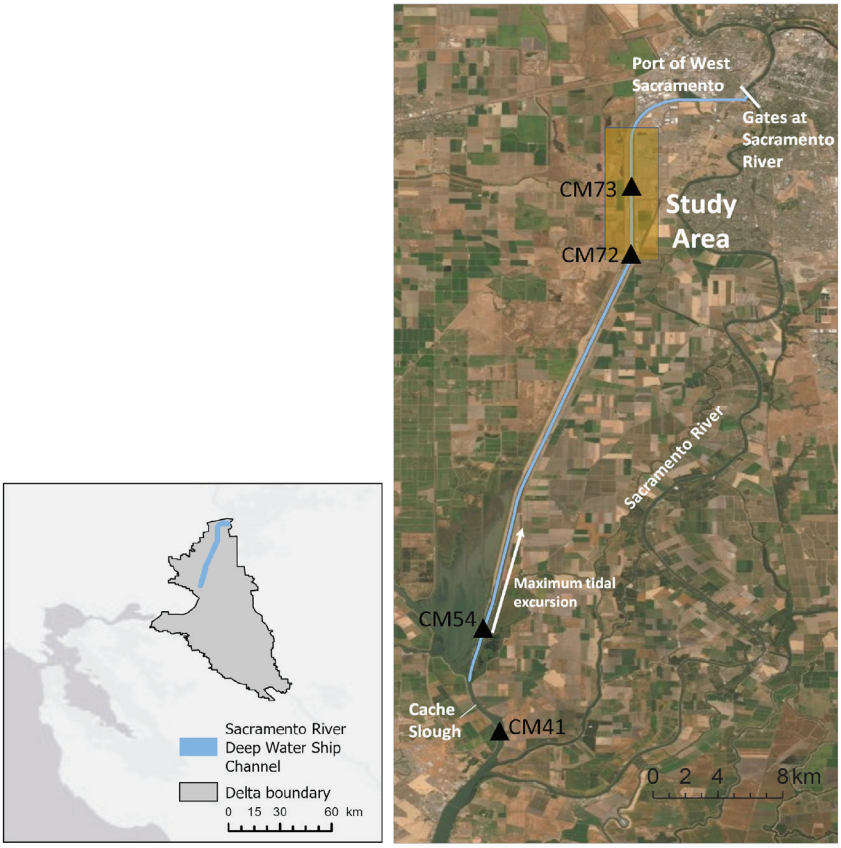

Figure 1 Study area (indicated by *yellow box*) in the Sacramento River Deep Water Ship Channel in the Sacramento–San Joaquin Delta

ecosystem, with phytoplankton production ranking in the lowest 15% of the world's estuaries (Cloern et al. 2014) and declining overall in recent decades (Robinson et al. 2016). The population decline of many fish species in the estuary is believed to be a response, in part, to the decrease in phytoplankton abundance through cascading effects in the rest of the food web (Sommer et al. 2007). Recent habitat-restoration efforts in the estuary have specifically focused on increasing primary production to support fish populations, several of which are listed as threatened or endangered species under Federal and California Endangered Species Acts (CDFW 2019).

Spatiotemporal variability in hydrodynamic processes can make it difficult to identify and then quantify the principal forcing mechanisms on phytoplankton dynamics and primary production. For example, physical processes such as wind and tidal currents that control mixing time-scales interact with nutrient concentrations, water temperature, and turbidity (affecting ambient light levels, heat fluxes, and thermal stratification), which together control spatial and temporal patterns of productivity in estuaries (Cloern 2001; Robinson et al. 2016; Wurtsbaugh et al. 2019). To develop viable management strategies to promote robust, resilient food webs and to support fish populations, a better understanding of how hydrodynamic processes regulate primary production is needed.

This paper focuses on understanding mixing driven by tidal currents and wind, and their effect on the strength and duration of thermal stratification in the upper Sacramento River Deep Water Ship Channel (DWSC) (Figure 1) as a control on phytoplankton production. Our study from July 2 to September 18, 2019 was conducted as part of a whole-ecosystem experiment that tested the extent to which nitrogen amendments made to the DWSC during a period of seasonally low nitrate concentration might stimulate increased rates of primary and secondary production (USBR 2018, 2019).

METHODS

Study Area

Situated in the freshwater tidal portion of the Delta, the DWSC provides seagoing vessels access to the Port of West Sacramento (Figure 1). The DWSC is tidally forced (tidal currents range from -0.62 to $+0.50\,m\,s^{-1}$) at its southern end where it connects to Cache Slough. At the northern end, a set of inoperable gates separates the DWSC from the Sacramento River. Although some water flows through these gates ($<1\,m^3\,s^{-1}$ measured on August 22, 2019, which may be greater when water levels in the Sacramento River are elevated during high flow), the DWSC generally functions as a terminal slough with negligible stream inflow. These conditions result in progressively dampened tidal currents moving landward and, for practical purposes, little to no net flow. The central half of the channel cross-section is dredged to ~10 m, with wide, shallow benches on each shoreline. The benches are <1 m deep at mean tide, and together make up one-third of the total channel width (Figure 2).

Although the DWSC is a completely human-made, engineered channel with straight and homogenous channel form, it exhibits unexpected habitat heterogeneity along its length (Young et al. 2021) that supports the endemic, endangered Delta Smelt (Sommer and Mejia 2013; Moyle et al. 2016). The DWSC has physical and biological characteristics typical of terminal sloughs that were common in the historic Delta before agricultural reclamation (Whipple et al. 2012). These characteristics include long residence times (Downing et al. 2016), episodic thermal stratification (Robinson et al. 2016), and a flood-dominant tidal current asymmetry that leads to a turbidity maximum (Morgan-King and Schoellhamer 2013) and increased abundance of pelagic organisms (Feyrer et al. 2017) in the middle reaches compared to elsewhere along the length of the DWSC.

Data Collection

Continuous Monitoring

An RDI Channel Master (600-kHz) side-looking acoustic Doppler current profiler (SL-ADCP) was deployed near CM73 (USGS 383019121350701) at

https://doi.org/10.15447/sfews.2021v19iss4art5

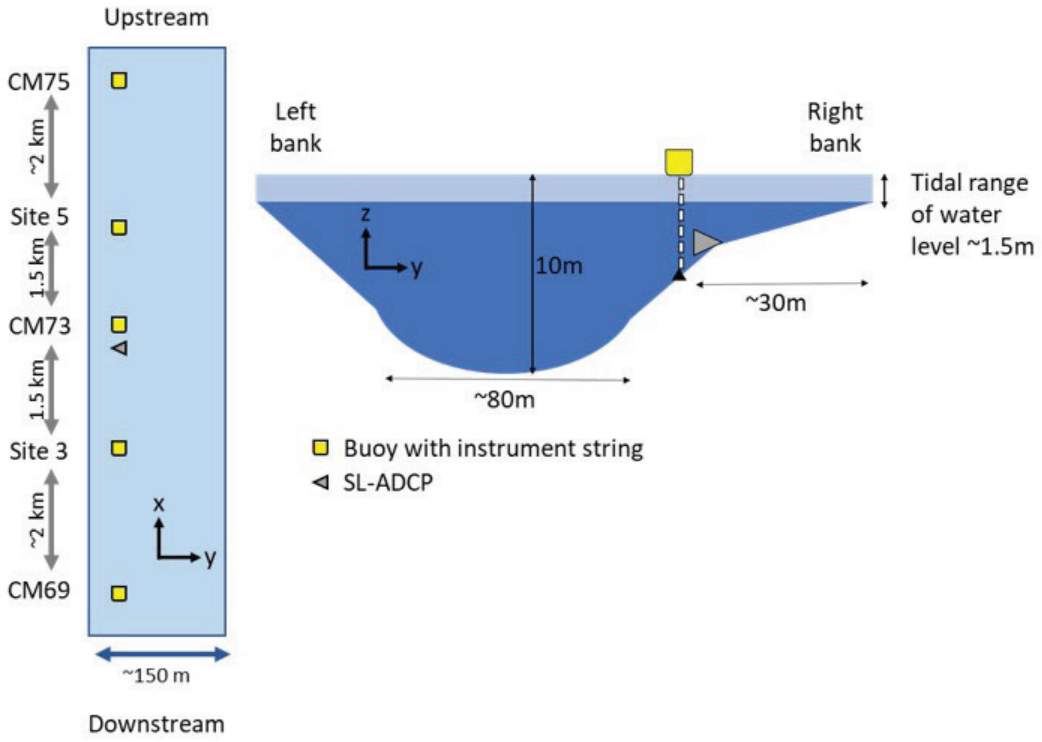

Figure 2 Monitoring network deployed in the study area and schematic of the channel cross-section, showing the deployment layout of sensors in the water column

2 m mean tidal depth to continuously measure water velocity and water level at 15-min intervals, and to compute discharge using the index velocity method (Ruhl and Simpson 2005) (Figure 2). We computed tidally averaged (or net) discharge using a Godin low-pass filter to remove tidal period variability (Godin 1972). Velocity and discharge records from long-term USGS monitoring stations near the study area—CM72 (USGS 11455095), CM54 near the mouth of the DWSC (USGS 11455335), and CM41 on Cache Slough (USGS 11455385) (USGS 2021)—are also used in this analysis and were similarly processed, following procedures detailed in Levesque and Oberg (2012) (Figure 1).

We deployed a network of instrument strings with sensors at multiple depths to monitor vertical stratification dynamics. Sensors were connected to cables held vertically on spar buoys at five locations longitudinally spaced throughout the study area (Figure 2). Each instrument string had three HOBO temperature probes, three HOBO conductivity/temperature probes, and three PME minidot dissolved oxygen/temperature probes located at 0.5-m increments below the water surface to 4.5 m deep. We deployed the instrument strings ~ 30 m from the right bank where water depth is ~ 5 m, so the instrument strings measure the equivalent of the top half of the total water column of the central channel. At CM73, we deployed an additional instrument buoy closer to shore that contained a YSI EXO2 sonde that measured temperature, specific conductance, dissolved oxygen, pH, turbidity, and chlorophyll-*a* fluorescence near the surface (USGS 383019121350701).

We deployed all instruments nearshore and tethered to land to avoid their destruction or removal from the study site by ships that traverse the DWSC an average of three times each week. Ships occupy most of the dredged width and depth of the channel, creating a large wake and significant prop wash that resuspends bed material. The signature of ship passage is apparent in the continuous turbidity data and confirmed by a camera placed at CM73 that collected an image every minute.

Synoptic Studies

We conducted short-term synoptic studies weekly for 4 weeks to evaluate the vertical and horizontal mixing dynamics. We collected four velocity transects each hour for 30 hours using an autonomous surface vessel (ASV) mounted with an RDI RiverPro (1200-kHz) down-looking ADCP (DL-ADCP) at the CM73 cross-section. We processed the transects with the Velocity Mapping Toolbox (VMT) (Parsons et al. 2013) in Matlab to remove erroneous values and produce average velocity profiles of along-channel and cross-channel velocities for each hour.

We also collected vertical water quality profiles hourly at the CM73 cross-section with a SonTek CastAway conductivity-temperature-depth instrument (CTD). We collected CTD casts of the entire water column at three points in the deep central channel. These measurements were collected at the same locations in each synoptic study. We processed the CTD measurements with the CastAway software package from SonTek to remove erroneous data, average samples from the down- and up-cast, and compute water density as detailed in the software user's manual (SonTek 2017).

Analytical Approach

Estimating mixing processes from data can be challenging, so we used (1) a variety of approaches to estimate mixing time-scales at our study site, (2) two metrics to quantify the level of stratification, and (3) an energy balance to determine the primary physical forcing that controls stratification and to examine the frequency of stratification over an 11-year period from 2009 to 2019.

Mixing

We followed the approach outlined in Geyer et al. (2008) for estimating time-scales of longitudinal (T_x), lateral (T_y), and vertical (T_z) mixing, where

$$T_x = \frac{L^2}{10K_x} \quad (1)$$

$$T_y = \frac{B^2}{10K_y} \quad (2)$$

$$T_z = \frac{h^2}{10K_z} \quad (3)$$

L is the longitudinal mixing length scale, which we defined as the median tidal excursion (2.09 km, computed from the continuous velocity data at CM73); B is the width of the channel (160 m); and h is the average depth (7.5 m).

We computed estimates of lateral dispersion (K_y) and vertical dispersion (K_z) from direct measurements. Longitudinal dispersion (K_x) was estimated using three different approaches, including using direct measurements and from bulk hydraulic parameters. Even with a conservative tracer, estimating longitudinal dispersion is difficult (Carr and Rehmann 2007); therefore, several approaches were used to provide confidence in our estimates. We chose these specific approaches because they represent distinctly different time-scales and mixing mechanisms.

The first approach estimated K_x from DL-ADCP profile data collected during the synoptic studies; this approach is referred to as the triple integral method (Fischer et al. 1979). Each DL-ADCP profile represents a ~30-min snapshot; thus, estimates using this approach are considered instantaneous. The calculation of K_{x1} is as follows:

$$K_{x1} = -\frac{1}{A}\int_0^B hU' \int_0^y \frac{1}{K_y h}\int_0^y hU'\,dy\,dy\,dy \quad (4)$$

where A is the cross-sectional area, B is the channel width, y is the coordinate in the cross-stream direction, h is the depth at location y in the cross-section, U' is the deviation of depth- averaged velocity at point y from the mean channel velocity (U), and K_y is the lateral dispersion coefficient. K_y is calculated based on the formula from Shen et al. (2010) as:

$$K_y = \left[0.145 = \left(\frac{1}{3520}\right)\left(\frac{U}{U_*}\right)\left(\frac{B}{h}\right)^{1.38}\right] U_* h \quad (5)$$

where U is the cross-sectionally integrated shear velocity (U=0.1U), which is the water

https://doi.org/10.15447/sfews.2021v19iss4art5

column integrated value for each ensemble, which represents a narrow vertical slice of the cross-section.

The triple integral method is not without its limitations. Past studies have shown that estimates based on ADCP data are generally accurate within only several orders of magnitude at best (Carr and Rehmann 2007). Nevertheless, Shen et al. (2010) showed that dispersion estimates from ADCP data can be a good alternative to using estimates from tracer data when multiple transects are taken at a single cross-section, because median values over multiple cross-sections yield closer agreement with tracer data. Furthermore, accuracy in K_{x1} is sensitive to the accuracy of K_y, and Carr and Rehmann (2007) showed that errors in K_{x1} will be largest when the velocity profile is nearly uniform, likely because deviations from the mean (U') are small.

The second approach estimated K_x from longitudinal nitrate transects, referred to here as the variance in the Gaussian fit method. After each of eight additions of calcium nitrate between July 22 and August 8, 2019, we produced longitudinal maps of surface nitrate concentrations using a boat-mounted, GPS-referenced, flow-through system configured with a Satlantic SUNA V2 optical nitrate sensor (Crawford et al. 2015; Downing et al. 2016). We collected successive nitrate transects about 20 hr apart (Lenoch et al. 2021), so these estimates of K_x are considered an integrated estimate over that interval.

The calculation of K_{x2} is as follows:

$$K_{x2} = -\frac{1}{2}\frac{d\sigma_x^2}{dt} \approx \frac{1}{2}\frac{\sigma_x^2(t_2) - \sigma_x^2(t_1)}{t_2 - t_1} \quad (6)$$

where σ_x^2 is the variance in the Gaussian fit to the nitrate concentration along the channel, and the time of the second and first profiles are t_2 and t_1, respectively. This approach assumes that the constituent used is conservative (i.e., there are no sources or sinks). Nitrate is not a conservative constituent; however, over the 20-hr time interval we expect minimal uptake of nitrate. We expect the upper bound of total ecosystem nitrate uptake to be on the order of 0.02 mg N L^{-1} d^{-1}, based on the maximum estimated nitrate uptake rate constant of 0.039 d^{-1} from a greater Delta study (Downing et al. 2016) and the targeted nitrate fertilization concentration of 0.5 mg N L^{-1}. The ecosystem nitrate uptake rate is small compared to the observed change in nitrate in the center of the fertilized area on successive days (~0.5 mg N L^{-1} d^{-1}) (Lenoch et al. 2021). In addition, dispersion is calculated using the shape (variance) of the spatial distribution, which makes it robust if non-conservative behavior is similar across the spatial domain.

Since the direct estimates of longitudinal dispersion given above were made over relatively short periods (0.5 to 20 hr) based on limited data, we also calculated dispersion estimates using bulk hydraulic parameters to determine if these estimates could be used for analysis over longer time-scales (tidal periods to years). The third approach is based on oscillatory tidal flows derived from depth, width, and mean velocity (Fischer et al. 1979), and, as such, is the easiest to obtain. This approach is referred to as the oscillatory tidal flow method. The calculation of K_x is as follows:

$$K_{x3} = 0.02U^2T\left[\left(\frac{1}{T'}\right)f(T')\right] \quad (7)$$

where U is the mean cross-sectional velocity averaged over a tidal period (T ~ 12.4 hr) from the SL-ADCP and T' is T/T_c where T_c is the time required for cross-sectional mixing. T_c is equal to T_y and is estimated using the K_y based on Equation 5 and T_y in Equation 2. T_c is an averaged value since there was no clear correlation between K_y and water velocity. This method assumes complete vertical and lateral mixing and can be thought of as the overall estuarine dispersion rate based solely on the tidal currents, which may be different than the actual effective dispersion rate based on additional dispersion mechanisms that are incorporated within the K_{x1} and K_{x2} estimates from direct measurements.

We estimated vertical dispersion (K_z) based on a formula from Fischer et al. (1979) and depth-integrated velocity shear from the DL-ADCP data. We used the following equation to initially estimate K_z:

$$K_{zi} = 0.0025\, h\, U \tag{8}$$

where h is the depth of the water and U is the mean over the tidal cycle of the mean cross-sectional velocity. To get instantaneous estimates with the DL-ADCP data, we assume velocity shear (dU/dz) will change values of K_{zi}. Water column-integrated velocity shear is calculated from cross-sectionally averaged streamwise velocity (U_a) (Fischer et al. 1979) as follows:

$$shear = \frac{1}{h}\int_0^h \frac{U_a}{dz}\, dz \tag{9}$$

The final estimate of K_z is then the shear scaled by the ratio of the averaged K_{zi} ($\overline{K_{zl}}$) and shear ($\overline{shear}$) as follows:

$$K_z = shear\, \frac{\overline{K_{zt}}}{\overline{shear}} \tag{10}$$

To investigate the influence of wind and tide on dispersion, we summarized instantaneous dispersion estimates in three dimensions. We categorized K_{x1}, K_y, and K_z by tidal phase (ebb tide defined as cross-sectionally averaged water velocity $> 0.05\,m\,s^{-1}$, slack tide within $0 \pm 0.05\,m\,s^{-1}$, and flood tide $< -0.05\,m\,s^{-1}$) and by wind speed (high wind $> 4\,m\,s^{-1}$ and low wind $\leq 4\,m\,s^{-1}$).

Stratification

We used two metrics to quantify density stratification and water column stability in the DWSC. The first is the potential energy anomaly (Φ; $J\,m^{-3}$) in the water column, or strength of stratification, relative to a vertically well-mixed condition (Simpson and Bowers 1981).

$$\Phi = \frac{1}{h}\int_{-h}^{0} (\hat{\rho} - \rho)\, gz\, dz \tag{11}$$

$$\hat{\rho} = \frac{1}{h}\int_{-h}^{0} \rho\, dz \tag{12}$$

$\rho(z)$ is the density profile of the water column, $\hat{\rho}$ is the depth-integrated density of the entire water column to depth (h), and g is the acceleration from gravity. We calculated ρ based on temperature and salinity from the instrument string sensors, using the *marelac* package (version 2.1.10, Soetaert and Petzoldt 2020) in R 4.0.0 (R Core Team 2020). Equations 11 and 12 were used for both the *in situ* instrument strings (Φ) and the CTD casts (Φ_C). The time-series of Φ for the duration of the study was corrected based on the regression with Φ_C collected during the synoptic studies to account for underestimation of the potential energy anomaly computed from the instrument strings relative to the full water column. The instrument strings were located out of the navigational channel and measured the upper 4.5 m, while the CTD casts were collected in the central channel over the entire water column depth (~10 m). We defined the duration of stratification as the number of hours each day (5 am to 5 am) where the potential energy anomaly exceeded 1 $J\,m^{-3}$. Although this threshold is subjective, it provides a consistent baseline for defining the presence and absence of stratification.

The second metric is the dimensionless gradient Richardson number (Ri), used to assess water column stability as a result of vertical density stratification (Monin and Yaglom 1972). Ri is computed as the ratio of the buoyancy frequency squared (N^2), a measure of the density stratification that stabilizes the water column—to the vertical shear squared ($S_h{}^2$), a measure of turbulence that acts to vertically mix the water column (Gill 1982):

$$Ri = \frac{N^2}{S_h^2} \tag{13}$$

$$N^2 = -\frac{g}{\rho}\frac{d\rho}{dz} \tag{14}$$

$$S_h^2 = \left(\frac{du}{dz}\right)^2 \tag{15}$$

https://doi.org/10.15447/sfews.2021v19iss4art5

The components of *Ri* were calculated hourly at 0.5-m depth intervals during the synoptic studies. The density gradients ($d\rho/dz$) were computed from the average of the three CTD casts, and velocity gradients (du/dz) from the average along-channel velocity of the deep central channel from the four DL-ADCP transects collected each hour. *Ri* was integrated with respect to depth to represent an hourly value of water column stability. Early publications defined a theoretical critical *Ri* value of 0.25, below which the water column is unstable (Miles 1961; Howard 1961), while subsequent researchers have argued for a critical *Ri* of up to 1, or that no critical value exists, considering the reality of turbulent, three-dimensional flow (Abarbanel et al. 1984; Galperin et al. 2007; Yamamoto 1975, Lettau 1979). Given the uncertainty of a critical value in the literature, we used an *Ri* threshold of 1 to interpret the relative importance of buoyancy versus shear in the water column.

Energy Balance

We computed expected changes in potential energy anomaly (Φ_M) by considering the forces that promote stratification (i.e., buoyancy from heating) and those mechanisms that cause the water column to mix vertically (i.e., tidal currents and wind). Equation 16 computes the change in potential energy anomaly in the water column over time as a function of heating and stirring (Simpson and Bowers 1981).

$$\frac{d\Phi_M}{dt} = \frac{\alpha g \dot{Q}}{2c_p} - \frac{4}{3\pi}\varepsilon k \rho_w \frac{u_1^3}{h} - \delta k_S \rho_S \frac{\overline{W^3}}{h} \qquad (16)$$

The first term on the right side of Equation 16 is surface heating from the net heat flux $\dot{Q}$ ($W m^{-2}$). The second and third terms are a result of stirring of the water column of depth h—10 m in this study—by a tidal current of amplitude u_1 and wind of speed W, respectively. ε and δ are the corresponding efficiencies of mixing, k and k_s are the effective drag coefficients for bottom and surface stresses, α is the thermal expansion coefficient, c_p is the specific heat of freshwater, and ρ_s is the density of air.

Heat flux at the air-water interface is a result of shortwave radiation ($\dot{Q}_W$), net longwave radiation ($\dot{Q}_{LW}$), latent heat ($\dot{Q}_{LH}$), and sensible heat ($\dot{Q}_{SH}$).

$$\dot{Q} = \dot{Q}_W + \dot{Q}_{LW} - \dot{Q}_{LH} - \dot{Q}_{SH} \qquad (17)$$

$\dot{Q}_W$ is a direct measurement. Heat fluxes from $\dot{Q}_{LW}$, $\dot{Q}_{LH}$, and $\dot{Q}_{SH}$ are calculated with Matlab routines described in Pawlowicz et al. (2001) using air temperature, barometric pressure, relative humidity, wind speed, and surface water temperature. Meteorological data were acquired from California Irrigation Management Information System (CIMIS) weather station 121 in Dixon, located 20 km from the study area.

The modeled potential energy anomaly (Φ_M) and each term in Equation 16 were integrated for time, starting from the onset of stratification. Integrated values below zero were set to zero, since additional mixing after the water column is well mixed is not important. The energy balance was also modeled using velocity and temperature data from CM54, which has a long-term record dating back to 2009. These data were scaled to represent conditions at CM73 and provide an estimate of the frequency and duration of stratification over a longer time-period.

RESULTS

The main drivers of transport and mixing in estuaries include the tidal currents, net advection, wind, gravitational circulation as a result of horizontal density gradients, and vertical density stratification (Fischer et al. 1979). Not all these processes are relevant in the DWSC. For example, net advection in the DWSC is negligible—below the noise threshold of what we can detect using boat-mounted DL-ADCP transects and time-series data from long-term flow stations. Similarly, the DWSC is located well upstream of salinity intrusion and does not exhibit two-layer gravitational circulation exchange flow, a physical process present in the brackish portions of the estuary where the horizontal salinity gradient can be much steeper (Monismith et al. 1996). There is a weak horizontal specific conductance gradient

in the DWSC primarily due to evaporation, from a minimum of ~100 µS cm^{-1} (0.05 psu) at CM54 to a maximum of ~900 µS cm^{-1} (0.45 psu) at CM72 (Feyrer et al. 2017), and specific conductance throughout the DWSC is well below the defined lower limit of 2 psu of the practical salinity scale (UNESCO 1981). Vertical density stratification in the estuary is dominated by salinity gradients and varies seasonally depending on Delta outflow (Vroom et al. 2017; Cloern 1996) and because of tidal current differences on spring and neap tide (Monismith et al. 1996), whereas salinity stratification in the Delta is generally absent, except in the confluence region where the Sacramento and San Joaquin rivers meet. Vroom et al. (2017) found that thermal stratification is present throughout San Francisco Bay and far less so in the Delta generally, though it is present at times in deep channels (Schladow and Monismith 2009) and in areas with low flow velocities, such as our study area. Thus, after the scaling analysis given above, the wind, tidal currents, and vertical temperature stratification remain as possible significant drivers of transport and mixing in the DWSC.

Atmospheric Forcing

Wind

Strong winds develop across the Delta during late afternoon and evening in the summer—the so-called "Delta breeze"—because of differential warming of air over the Pacific Ocean and in the California Central Valley (Frenzel 1962; Zaremba and Carroll 1999). During the study, the wind speed typically increased around 16:00 PST each day, a statistically significant increase over the mean wind speed of the previous hour, and wind speeds remained elevated through the evening. Since we are most interested in how wind influences on stratification, we selected 16:00 until sunset as the analytical period of interest for wind effects because the solar radiation that acts to build thermal stratification ceases at sunset.

Wind speeds in the late afternoon and evening are significantly higher than other times of day, with a mean wind speed of 4.16 m s^{-1} in the evening compared to 2.94 m s^{-1} at other times of the day (Welch Two Sample t-test; p-value < 0.001). Lower-magnitude winds occur about 25% of the time in both periods, but wind speeds greater than 4 m s^{-1} occur more frequently during later afternoon and evening (Figure 3A), about 50% of the time, compared to other times of day (Figure 3B). Wind direction during the study period (July to September) was consistently from the south-southwest, aligning predominantly with the channel orientation and coinciding with the current direction on flood tide, with slightly more variability in wind direction outside of late afternoon and evening.

Heat Flux

The components of the heat flux—water temperature and air temperature, atmospheric pressure, and wind speed (Figure 4A-C)—show variability of atmospheric conditions throughout the study and their effect on the net heat flux at the air-water interface (Figure 4D). There is strong correlation between high air temperature, low wind speed, and elevated net heat flux.

Tidal Currents

The magnitude of tidal currents varies along the length of the DWSC (Figure 5), with velocities reduced by about a factor of 2.75 in our study area on average, ranging from −0.39 to +0.30 m s^{-1} at CM73, compared to currents of −0.62 to +0.50 m s^{-1} at CM54. Tidal currents are even stronger outside of the DWSC, ranging from −0.75 to +0.76 m s^{-1} in Cache Slough near Rio Vista at CM41 over the duration of our study.

Tidal currents in the DWSC are flood dominant, with peak flood velocities nearly double the maximum ebb on any given cycle—a tidal asymmetry observed in many estuaries where the currents become more flood dominant farther upstream (Dronkers 1986; Woodroffe 2002). Flood dominance occurs in the DWSC as the tide wave transitions from progressive wave in the seaward Delta to standing wave farther landward as a result of reflection off the end of the terminal channel, with high and low tide occurring near slack water (Walters et al. 1985; Hoitink and Jay 2016). Conservation of mass (the net flow is zero in our study area) requires shorter, faster flood tides compared to longer, slower ebb tides

https://doi.org/10.15447/sfews.2021v19iss4art5

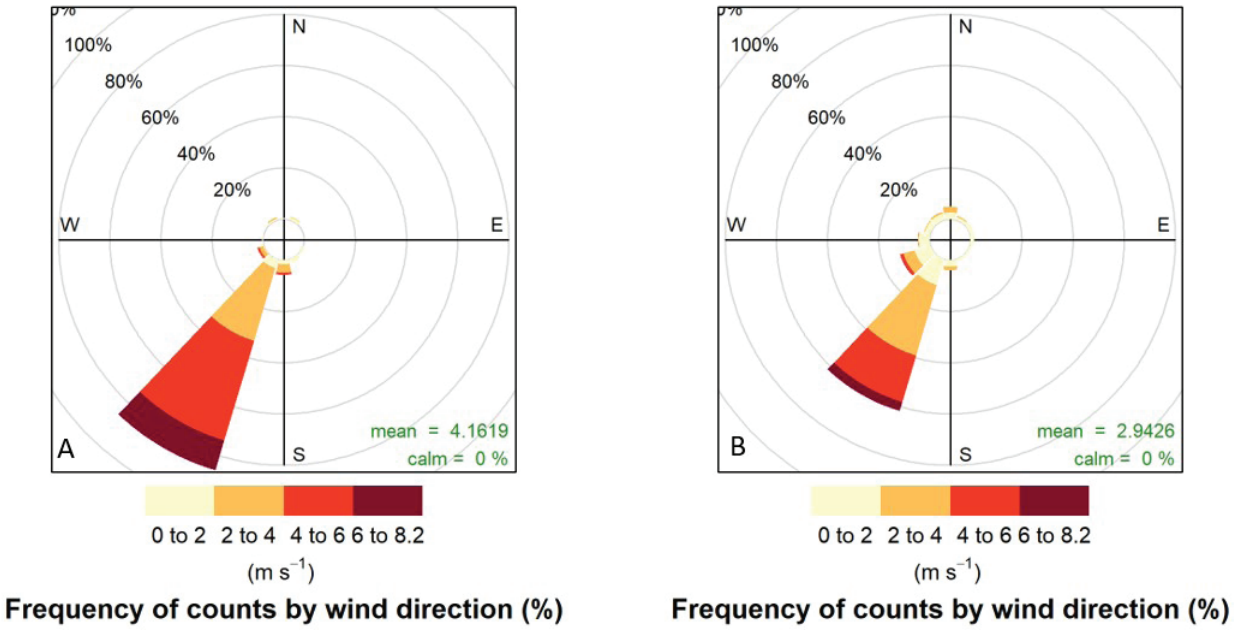

Figure 3 Wind rose summarizing hourly wind speed (m s^{-1}) and frequency of counts (%) by meteorological wind direction during (**A**) late afternoon and evening (16:00 to sunset) compared to (**B**) all other times of day over the experiment (7/2/19 to 9/18/19) from the Dixon weather station (CIMIS ID 121)

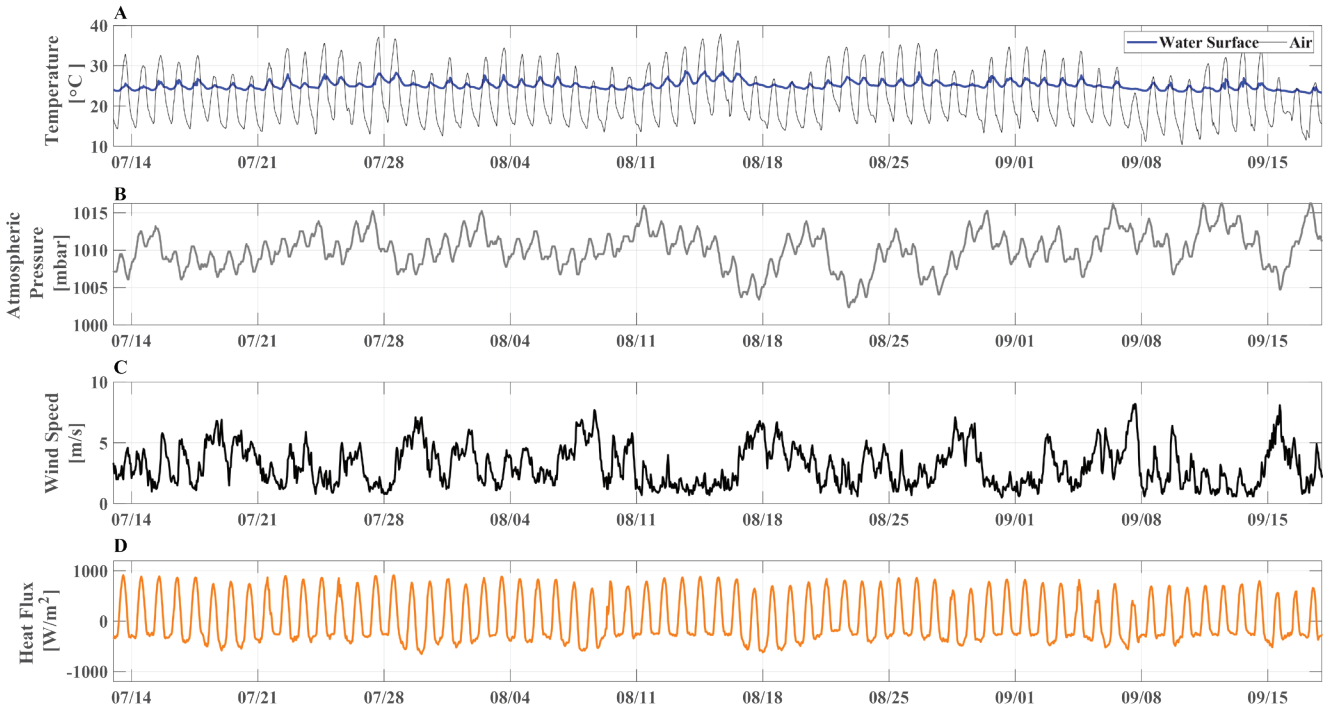

Figure 4 Components of the heat flux calculation (Equation 17): (**A**) water temperature (*blue*), air temperature (*black*), (**B**) atmospheric pressure, (**C**) wind speed, and (**D**) net heat flux. Meteorological data are from CIMIS station 121 in Dixon, CA.

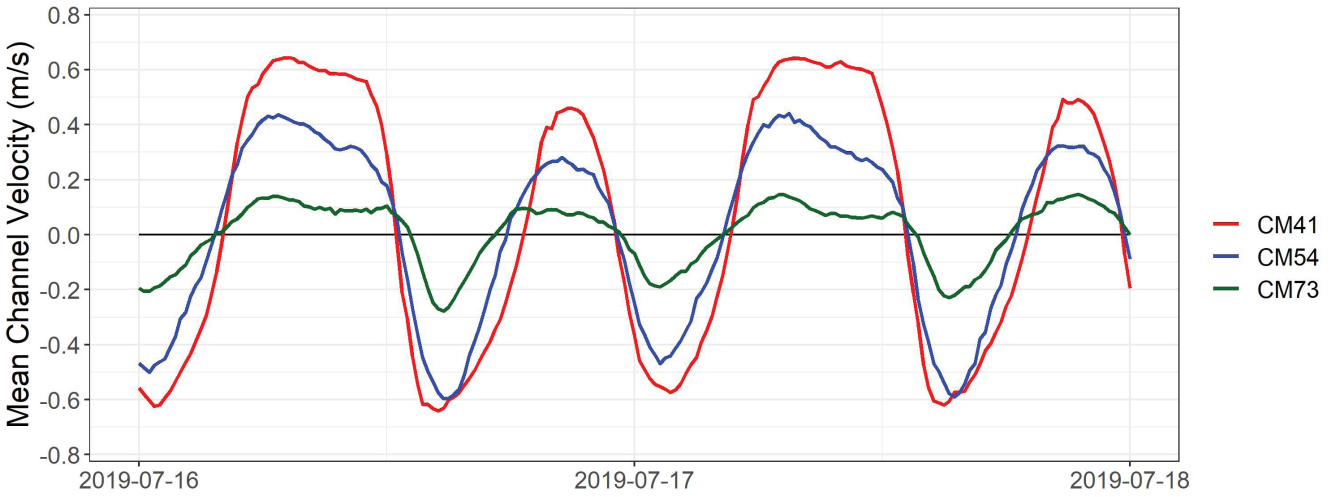

Figure 5 Comparison of tidal currents in the study area (CM73), at the southern end of the DWSC (CM54), and in Cache Slough (CM41). Flood tidal currents are negative; ebbs positive.

because the depth—and consequently cross-sectional area—is less during floods over ebb tides (e.g., CM73 in Figure 5).

The strength of the tidal currents in the DWSC dominate both longitudinal mixing (tidal excursions on the order of 2 to 4 km at CM73 and 6 to 10 km at CM54 near the mouth of the DWSC) and transverse dispersive mixing, driven by significant sidewall boundary layers that extend from each bank across the shallow benches. Vertical mixing is similarly driven by tidal mixing, with wind-enhanced mixing occurring at the surface balanced against thermal stratification that tends to stabilize the water column.

We used hourly velocity profiles collected during the synoptic studies to investigate longitudinal, lateral, and vertical dispersion estimates, time-scales of mixing, and how wind shear and thermal stratification affect vertical dynamics. The along-channel velocity (U) profiles illustrate that vertical gradients in along-channel velocity, or shear (dU/dz), penetrated from the surface with the onset of wind in the afternoons: near-surface shear was generally weak outside of afternoon and evening hours, independent of current direction. For example, the velocity profiles in Figure 6 were collected during the late afternoon/evening period when wind speeds were elevated (average wind speed of 4.2 m s^{-1} during the measurement in Figure 6A and 4.6 m s^{-1} during the measurement in Figure 6B). The near-surface velocity was accentuated on the flood tide when the tidal current and wind were in the same direction (Figure 6A), whereas the near-surface velocity was slowed or stalled because of wind-generated shear at the surface in opposition to the ebb tidal current direction (Figure 6B).

Dispersion Estimates

Instantaneous rates of longitudinal, lateral, and vertical dispersion were influenced by tides and wind (Figure 7). Ebb tide and high wind produced the highest estimates of K_{x1} (Figure 7A). During slack and flood tides, K_{x1} was similar during both low and high wind conditions. K_y was highest on the flood tide and slightly higher during high winds (Figure 7B). During ebb and slack tides, K_y was similar during low and high wind conditions. K_z was highest during high wind conditions for all three tidal phases (Figure 7C). An example of this is shown in Figure 6: when the wind opposes the ebb tide there is higher shear in the water column (as opposed to the condition with the same water speed but less wind; not shown), which increases vertical (K_z) and longitudinal (K_{x1}) dispersion. The observed increase in shear was caused by the wind interacting with the vertical density

https://doi.org/10.15447/sfews.2021v19iss4art5

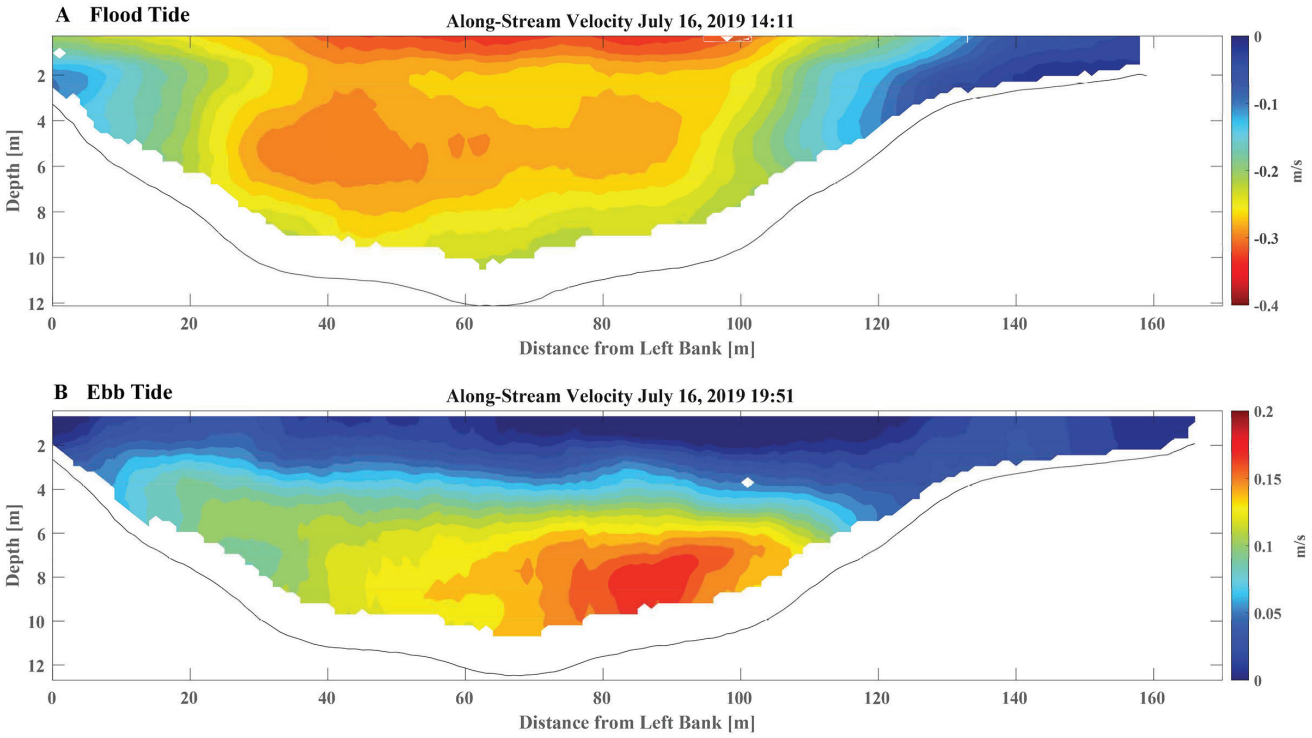

Figure 6 Examples of velocity profiles during (**A**) flood tide with the wind (wind speed 4.2 m s^{-1}) and (**B**) ebb tide opposing the wind (wind speed 4.6 m s^{-1}), showing the effect of elevated wind in the late afternoon and evening on near-surface velocities

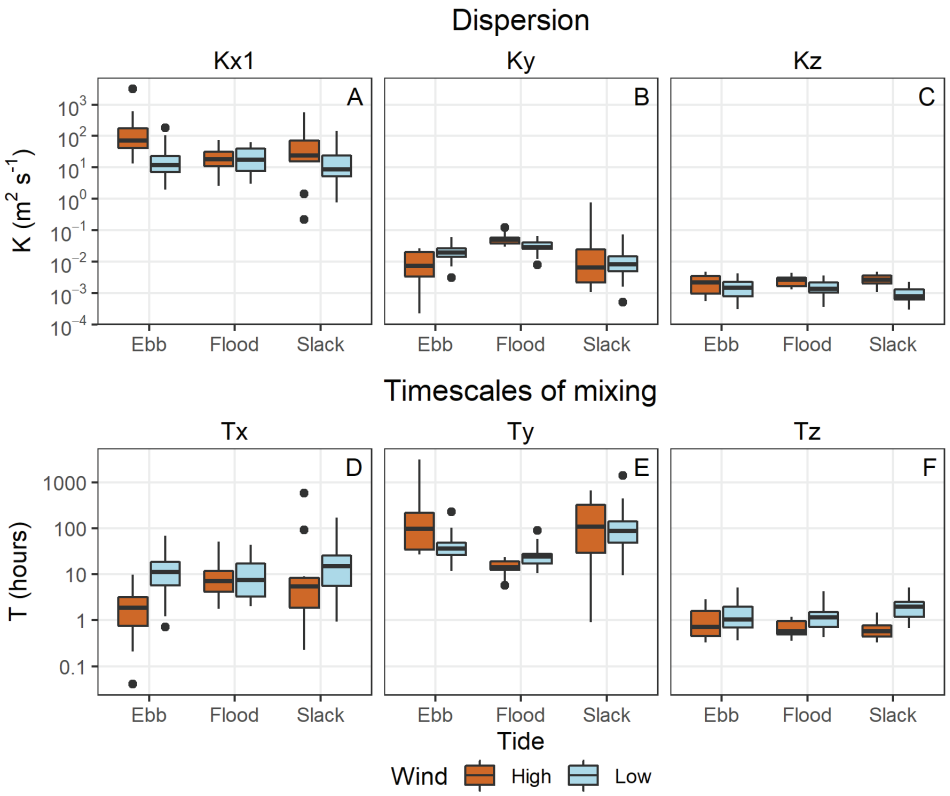

Figure 7 Estimates of longitudinal, lateral, and vertical dispersion (**A-C**) and time-scales of mixing (**D-F**) over the synoptic study periods

Table 1 Comparison of longitudinal dispersion estimates ($m^2\ s^{-1}$), with average wind speed ($m\ s^{-1}$) of the interval included for reference. K_{x2} was estimated when the nitrate maps were available (intervals 13-19).

Interval	Start Time	End Time	Duration (hours)	K_{x1}[a]	K_{x2}	K_{x3}[b]	Wind Speed[b]
1	07/16/2019 03:40	07/16/2019 17:14	13.57	10	—	10	2.51
2	07/16/2019 17:14	07/17/2019 04:16	11.03	18	—	3	4.17
3	07/17/2019 04:16	07/17/2019 18:09	13.88	7	—	8	1.81
4	07/23/2019 03:48	07/23/2019 15:51	12.05	58		3	3.14
5	07/23/2019 15:51	07/24/2019 05:11	13.33	10	—	5	3.24
6	07/24/2019 05:11	07/24/2019 16:26	11.25	9	—	2	2.05
7	07/29/2019 21:03	07/30/2019 12:00	14.95	20	—	7	5.41
8	07/30/2019 12:00	07/30/2019 21:48	9.8	43	—	5	3.83
9	07/30/2019 21:48	07/31/2019 12:40	14.87	6	—	7	2.44
10	08/06/2019 04:22	08/06/2019 16:47	12.41	17	—	8	2.26
11	08/06/2019 16:47	08/07/2019 05:42	12.92	17	—	4	4.22
12	08/07/2019 05:42	08/07/2019 16:33	10.85	32	—	4	4.45
13	07/22/2019 01:31	07/23/2019 07:01	19.49	—	19	6	2.53
14	07/23/2019 11:12	07/24/2019 06:55	19.72	18	13	4	3.34
15	07/24/2019 11:02	07/25/2019 07:27	20.42	—	15	3	1.77
16	07/25/2019 11:30	07/26/2019 07:16	19.77	—	30	7	3.57
17	08/06/2019 11:37	08/07/2019 07:28	19.86	14	18	6	3.82
18	08/07/2019 11:46	08/08/2019 07:34	19.79	—	15	4	5.75
19	08/08/2019 11:19	08/09/2019 07:29	20.16	—	12	3	4.79

a. Median value over interval period
b. Average value over interval period

profile, compared to periods of low wind (further explanation included in the analysis below). Most of the higher values of vertical shear occurred in the afternoon when the top layer of water (~3 m) is lighter (warmer) and the water column is stratified. Thermal stratification decouples the surface layer from the balance of the water column so the wind can independently move the surface layer because it does not have to overcome the inertia of the entire water column.

Longitudinal dispersion estimates from all three methods—triple integral (K_{x1}), Gaussian fit (K_{x2}) and oscillatory tidal flow (K_{x3})—are compared in Table 1. Estimates of K_{x3} were computed over a tidal cycle (~12.5 hr), and K_{x2} was computed over an interval of ~20 hr; therefore, the median values of K_{x1} were computed over these time intervals. Generally, estimates of K_{x1} and K_{x2} were higher than K_{x3}, suggesting that mechanisms other than oscillatory tidal flow (K_{x3}) aid in longitudinal dispersion. There are some periods when K_{x1} and K_{x3} are in close agreement and the wind speed for these intervals was low, but this correlation was weak. Other mechanisms such as tidal pumping and tidal trapping on the shallow benches are difficult to constrain, but either one may account for additional dispersion not captured in the formula for K_{x3}. The two intervals (14 and 17) for which both K_{x1} and K_{x2} existed showed that these estimates were similar (K_{x1} = 18 and 14 $m^2\ s^{-1}$; K_{x2} = 13 and 18 $m^2\ s^{-1}$). The overall average estimates of K_{x1} and K_{x2} from Table 1 are also similar: 20 and 17 $m^2\ s^{-1}$, respectively.

In summary, K_{x1} and K_{x2} appear to more accurately estimate longitudinal dispersion than K_{x3}. K_{x2} is based on direct measurements of nitrate (tracer method) dispersed at the study site, assuming the rate of dispersion is much greater than the uptake rate. Taking the reciprocal of the upper bound NO_3–N uptake rate 0.039 d^{-1} (from

https://doi.org/10.15447/sfews.2021v19iss4art5

Downing et al. 2016) implies the time-scale of NO_3 uptake is ~25 days, which is at least an order of magnitude slower than the average time-scale of dispersion over the tidal excursion length (~0.5 d, see below). The ADCP estimate of dispersion (K_{x1}) is considered accurate if it is in close agreement with a tracer-based method (K_{x2}) (Shen et al. 2010), which is the case at our study site. There is evidence that longitudinal dispersion increased on ebb tides when higher wind opposed the current direction, creating more vertical shear in the water column. Additional mechanisms, such as tidal trapping along the shallow benches, may also increase longitudinal dispersion.

Time-Scales of Mixing

Time-scales of mixing enable insight because they can uncover the effect of tidal phase and wind on mixing, and how fast constituents—in particular nutrients—disperse at our study site. We estimated mixing time-scales from the instantaneous estimates of dispersion based on DL-ADCP-derived calculations (K_{x1}, K_y, and K_z).

Time-scales of longitudinal mixing (T_x) had a median duration of 8.4 hr where variability was driven by the correlation between the current tidal phase and wind speed (Figure 7D). In general, T_x was higher when there was low wind for every phase of the tide, and the lowest T_x occurred during ebb tide with high wind. Time-scales of lateral mixing (T_y) had a median duration of 34.4 hr, and also reflected the correlation between the tidal currents and wind; however, T_y was actually higher during high wind on ebb and slack tides (Figure 7E). Overall, T_y was lower during flood tides, suggesting that the fastest lateral mixing occurred during flood tide periods. The time-scales of vertical mixing (T_z) had a median duration of 1.1 hr and were lower than both T_x and T_y, suggesting vertical mixing happens faster than horizontal mixing. Similar to longitudinal mixing, T_z was lower during high wind for every phase of the tide (Figure 7F). There were minimal differences in T_z among tidal phases, suggesting that time-scales of vertical mixing were primarily driven by wind speed.

Vertical Dynamics

The interaction of wind and tidal currents that act to mix the water column control vertical dynamics, while heat flux at the water surface creates stratification that reduces vertical mixing. These opposing mechanisms alternate in dominance, depending on the tidal current phase, wind speed, and the stability of the water column. Vertical stratification varied in magnitude and duration throughout the study (Figure 8). The different types of instruments that measured temperature throughout the water column had subtle intercalibration differences, so the vertical temperature profiles were smoothed (Figure 8A). However, the integration of Φ for the water column makes the stratification results resilient to these relatively minor instrumentation differences. Results from the central CM73 instrument string are presented; the vertical and temporal dynamics of stratification at all five instrument strings were comparable.

Surface water temperature increased daily as a result of heat flux from elevated air temperature and solar radiation. Generally, the daily heat flux was constrained to the upper 2 m of the water column, because of large light extinction coefficients, which averaged 1.75 m^{-1} (Loken et al. 2021; Lenoch et al. 2021). Deeper sensors did not exhibit much diurnal variability, but rather recorded higher temperatures when warmer water from the surface mixed downward (Figure 8A). The magnitude of temperature difference from the surface sensor to the sensor at 4.5 m depth was 0.97 °C on average (SD = 0.78 °C), with a maximum top-to-bottom difference of 4.43 °C measured during a period of strong stratification. Specific conductance values fluctuated semidiurnally with the tidal currents as a result of a longitudinal specific conductance gradient in the DWSC, but vertical variability in the water column was minimal (8 ± 22 µS cm^{-1} from surface to 4.5 m depth).

Changes in water temperature were the dominant control on vertical variability in density. Temperature and salinity influence density at different rates: a change in water temperature of 1 °C results in the same change in density as 0.2

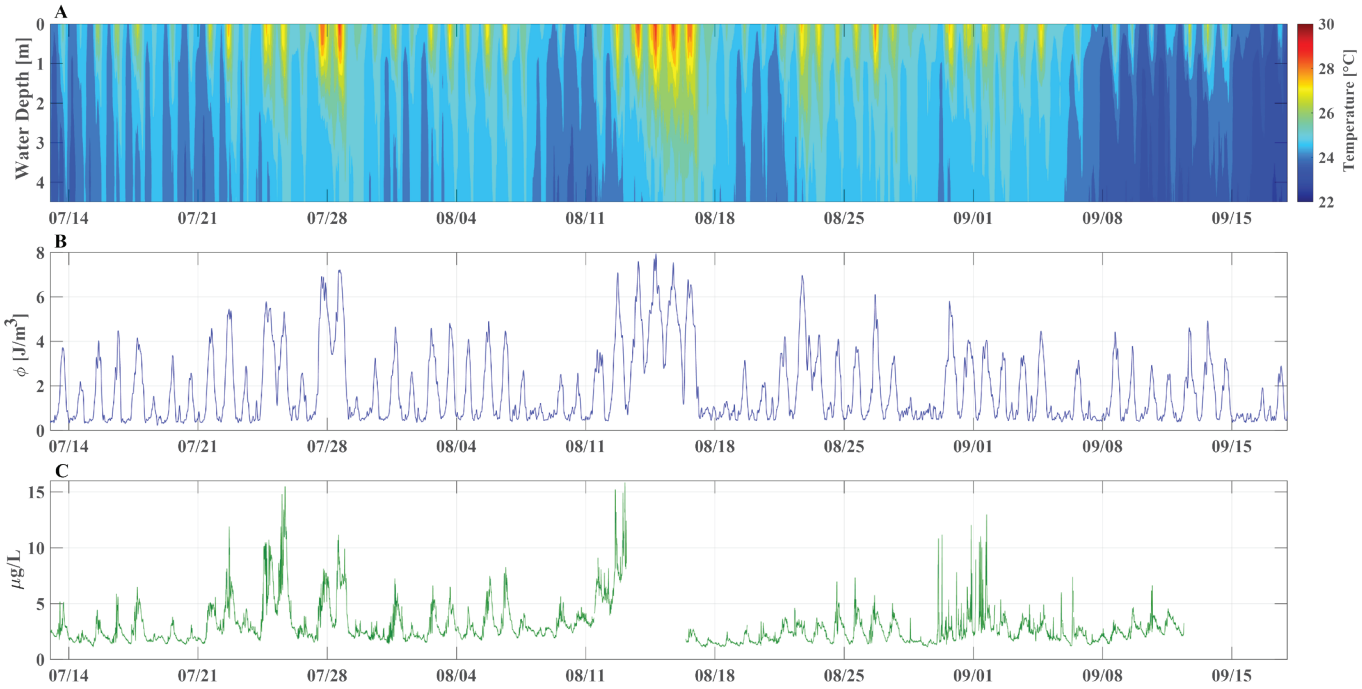

Figure 8 (**A**) Water temperature, (**B**) potential energy anomaly (Φ) from water surface to 4.5 m depth, and (**C**) chlorophyll-*a* concentration at CM73. Missing chlorophyll-*a* data resulted from sensor fouling.

psu change in salinity, equivalent to a specific conductance change of ~414 µS cm^{-1} (Geyer and Ralston 2011). Given the vertical gradients of temperature and specific conductance measured at CM73, vertical dynamics in temperature had a 14 to 50 times greater effect on density than changes in conductivity.

Temperature-driven stratification generally started around 10:30 PST each day and broke down each evening. Occasionally, stratification persisted overnight, and one event lasted multiple days in mid-August (August 13-16, 2019) (Figure 8B). Of the 78 days of record, there were only 5 days when stratification persisted overnight. There was no significant thermal stratification (defined as duration >2 hr) on 14 days. Thus, on most days (n=60), stratification developed and broke down, with average duration of 11.8 hr (SD = 5.9 hr) over the study period. Chlorophyll-*a* concentration increased daily, and greater increases tended to occur on days with strong or sustained stratification (Figure 8C).

Concurrent calculations of potential energy anomaly from the instrument string (Φ) and the hourly CTD casts from the synoptic studies (Φ_C) were well correlated (Figure 9A). We corrected the potential energy anomaly from the instrument string based on the regression formula (Figure 9A) to account for underestimation, and based on this correction Φ trended well with Φ_C and reasonably captured the peaks in stratification (Figure 9C-F). In general, the instrument string captured the vertical variability of the water column, but at times still underestimated the magnitude of stratification. Φ_C, and therefore Φ, does not go completely to zero because the water column does not perfectly mix to a uniform temperature, given the accuracy of the thermistors measuring to 0.01 °C. Values below 1 J m^{-3} can be considered well mixed.

The *Ri* analysis shows the development and evolution of stratification and shear in the water column (Figure 10). High values of *Ri* represent a stable water column, either from strong stratification or from very low to zero shear, often occurring near periods of slack water. In synoptic

https://doi.org/10.15447/sfews.2021v19iss4art5

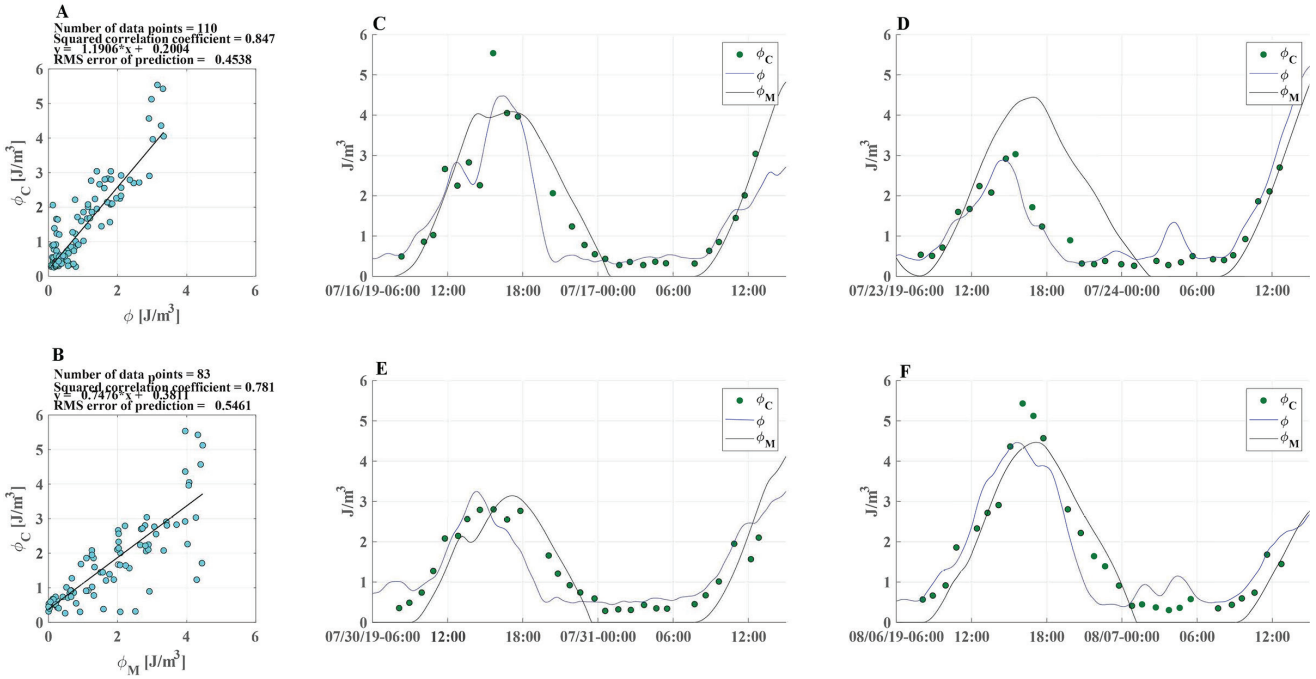

Figure 9 Comparison of potential energy anomaly from CTD casts (Φ_C), from the instrument string (Φ), and from the energy balance model (Φ_M). (**A**) Regression plot between Φ and Φ_C, and (**B**) between Φ_M and Φ_C, (**C-F**) time series plots from the synoptic studies.

study 1, density stratification developed in the top 2 m early in the day, reaching ~5 m in the late afternoon, and the velocity profile showed little variability (Figure 10A). The buoyancy from stratification (N^2) far surpassed shear ($S_h{}^2$) throughout the depth in the late morning and early afternoon, elevating values (Figure 10B and 10C). However, shear began to develop at the surface with the onset of higher winds exceeding 4 m s^{-1} around 15:00, with Ri decreasing rapidly over the next few hours as the shear overtook buoyancy. The increased shear from the wind combined with the decreased heat flux in the evening to vertically mix the water column from the surface in ~5 hr. In contrast, in synoptic study 2, shear was higher throughout the day as a result of sustained wind speeds of at least 3 m s^{-1}. The resulting shear component exceeded the buoyancy, maintaining low Ri values throughout the afternoon (Figure 10E and 10F), and preventing the development of strong stratification (Figure 10D).

Comparing synoptic studies 1 and 2 highlights the effects of wind and currents on stratification. During synoptic study 1, shear began to increase when the wind was ~4 m s^{-1} (Figure 10B); in synoptic study 2, shear increased at a lower wind speed of ~3 m s^{-1} (Figure 10E). This difference in response is attributed to the earlier onset of higher wind and weaker overall stratification during synoptic study 2. Additionally, the early afternoon increase in wind speed started during an ebb tide when the current was in opposition to the wind, which appears to enhance vertical mixing at similar values of vertical shear. Stronger stratification developed during synoptic study 1 even during flood tide, with flood velocities roughly double the ebb current velocity, showing that the correlation between the wind speed and current direction can more strongly influence the breakdown of stratification than tidal current magnitude alone.

Energy Balance

We used an energy balance to explicitly understand the effect of mixing from wind and tides in breaking down stratification relative to the creation of stratification through surface heating. This approach allowed us to compare

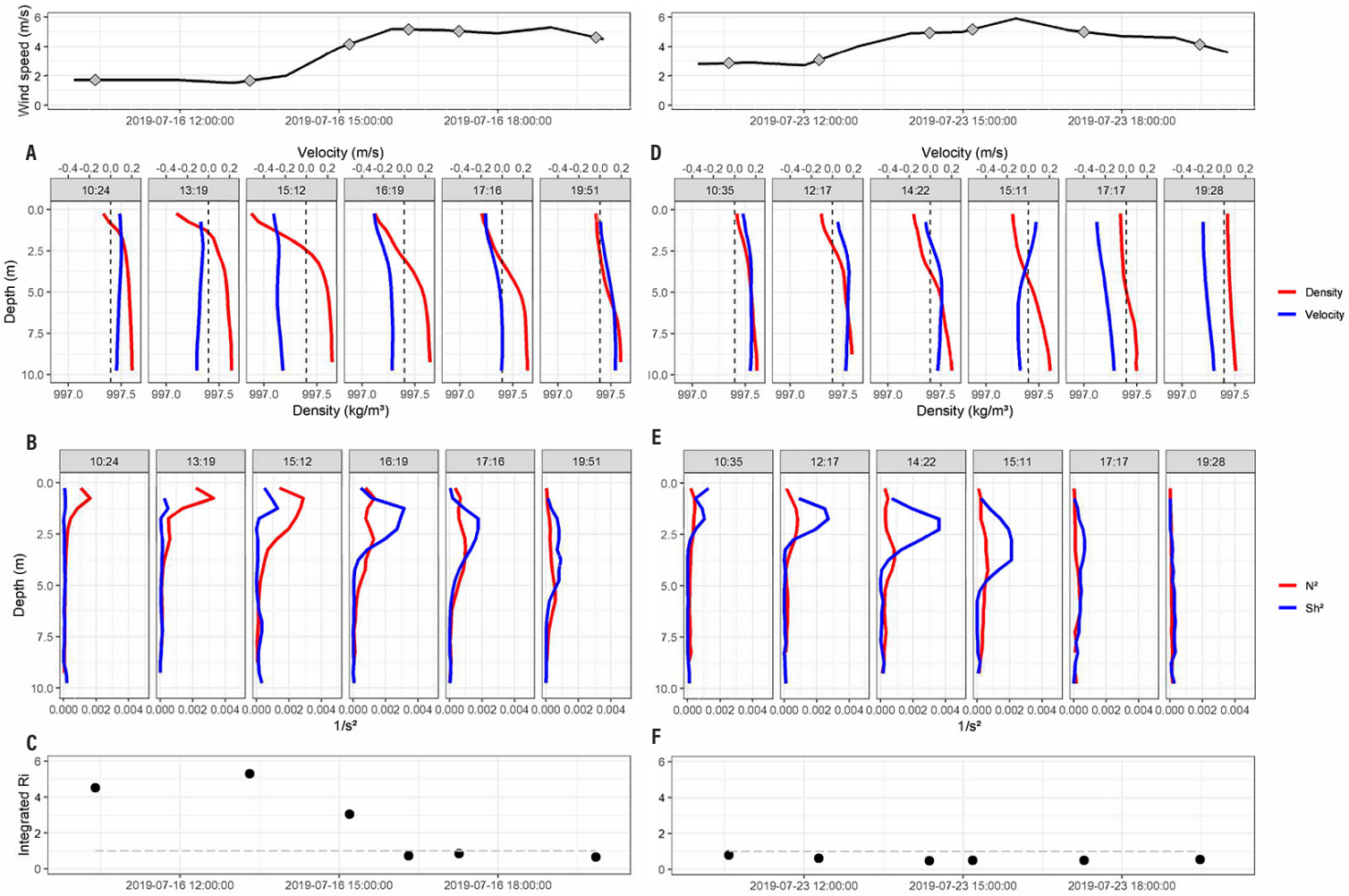

Figure 10 Vertical profiles of density and velocity (**A,D**), the components of (**B,E**), and depth-integrated values of (**C,F**) from synoptic studies 1 (Jul 16-17, 2019) and 2 (Jul 23-24, 2019). Ebb velocities are positive; flood velocities are negative. The *gray diamonds* on the **top panels** indicate wind speed (m s^{-1}) at each measurement time included in panels **A-F**.

the field measurement-derived calculations of potential energy anomaly from the instrument string (Φ) and CTD casts (Φ_C) in Equation 11 to the modeled potential energy anomaly of the water column based on atmospheric conditions and tidal mixing from Equation 16. Comparing and allowed us to refine the model to ensure it accurately represented the magnitude and duration of stratification measured during the synoptic studies. Mixing efficiencies for water velocity (ε) and wind (δ) were initially set to values from Simpson and Bowers (1981) of $\varepsilon = 0.0037$ and $\delta = 0.023$. Tuning these efficiencies based on regression between Φ_M and Φ_C (Figure 9B) resulted in values of $\varepsilon = 0.0111$ and $\delta = 0.069$. Overall, Φ_M performed well at Φ_C predicting ($R^2 = 0.78$, root mean squared error [RMSE] = 0.55). During synoptic studies 1 and 4, Φ_M underpredicted the peak in Φ_C (Figure 9C and 9F), during study 2, Φ_M overpredicted Φ_C during the late afternoon and evening (Figure 9D),

https://doi.org/10.15447/sfews.2021v19iss4art5

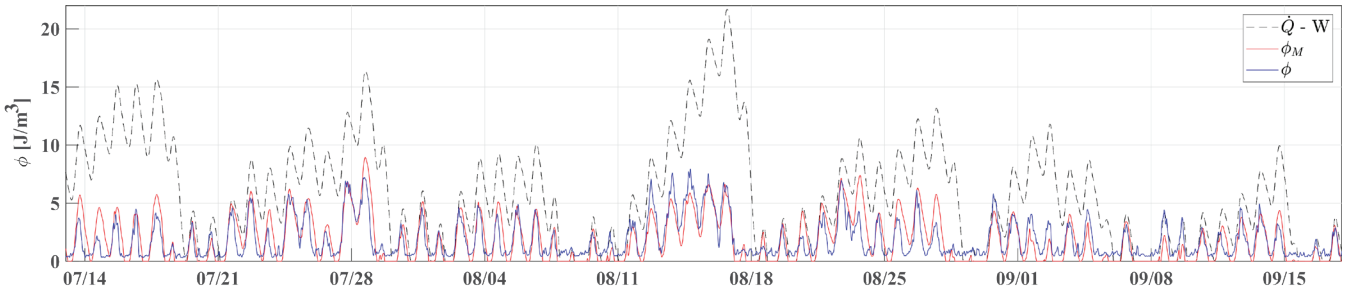

Figure 11 Comparison of potential energy anomalies: modeled from heat flux (*dashed orange*), modeled from heat flux and wind (*dashed black*), Φ_M modeled from all energy balance components (*red*), and measured Φ (*blue*)

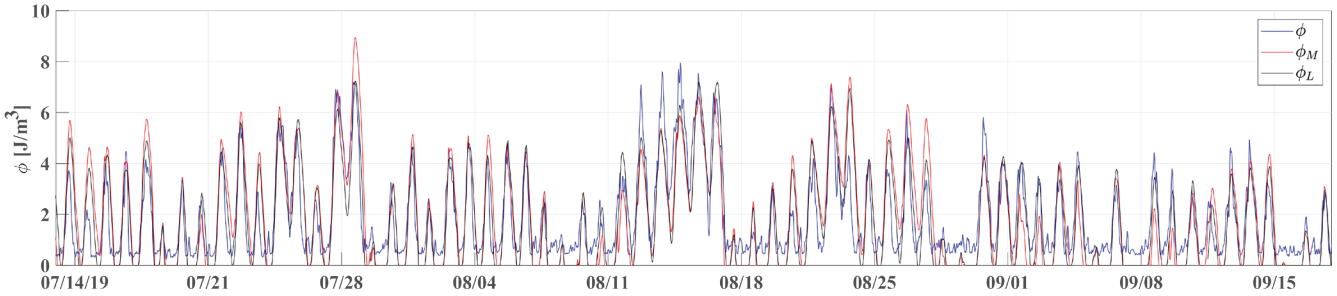

Figure 12 Potential energy anomaly calculated from instrument string (Φ, *blue*), energy balance model based on data from study period (Φ_M, *red*), and energy balance model based on long-term record (Φ_L, *black*) at CM73

and during synoptic study 3, Φ_M well predicted Φ_C (Figure 9E).

We sequentially added each term to the energy balance model to better understand how each mechanism affected the overall energy balance, and to compare to the time-series of Φ measured throughout the study (Figure 11). Potential energy anomaly in the water column is driven mainly by the heat flux and wind because these terms predicted the general trend of Φ, but stratification could not be sustained during most periods of low wind because of the tidal currents. Incorporating all terms (heat flux, wind, and water velocity), was well predicted by Φ_M (R^2 = 0.69, RMSE = 1.17), but during some periods of low wind (end of July and mid- to late-August) Φ_M overpredicted Φ. Increasing the mixing efficiency for water velocity (ε) provided a better prediction during these periods, but regression statistics of Φ_M to Φ_C decreased R^2 and increased the RMSE. Since Φ_C is our best estimate of potential energy anomaly because it measures the full water column, and there is evidence that Φ underpredicts peaks of Φ_C (see Figure 9C and 9F), we kept ε = 0.0111. On average, the difference in the duration of stratification between Φ_M and Φ was 0.32 hr (SD = 3.78 hr). It may be possible to improve upon the energy balance by incorporating more sophisticated time-variable mixing efficiencies (Burchard and Hofmeister 2008), but overall the model successfully predicted the general trends in stratification during our study period and was useful in examining the longer-term trends.

Analysis of Long-Term Record

To put our study period in context, we calculated the energy balance from an 11-year data record based on water temperature and velocity data from CM54, adjusted to represent conditions at CM73. Water velocity was on average about 2.75 times higher at CM54, and was scaled by 0.36 to reflect conditions at CM73. We did not correct water temperature because of poor correlation; rather, we calculated heat flux ($\dot{Q}_{54}$) with water temperature at CM54, which produced a bias

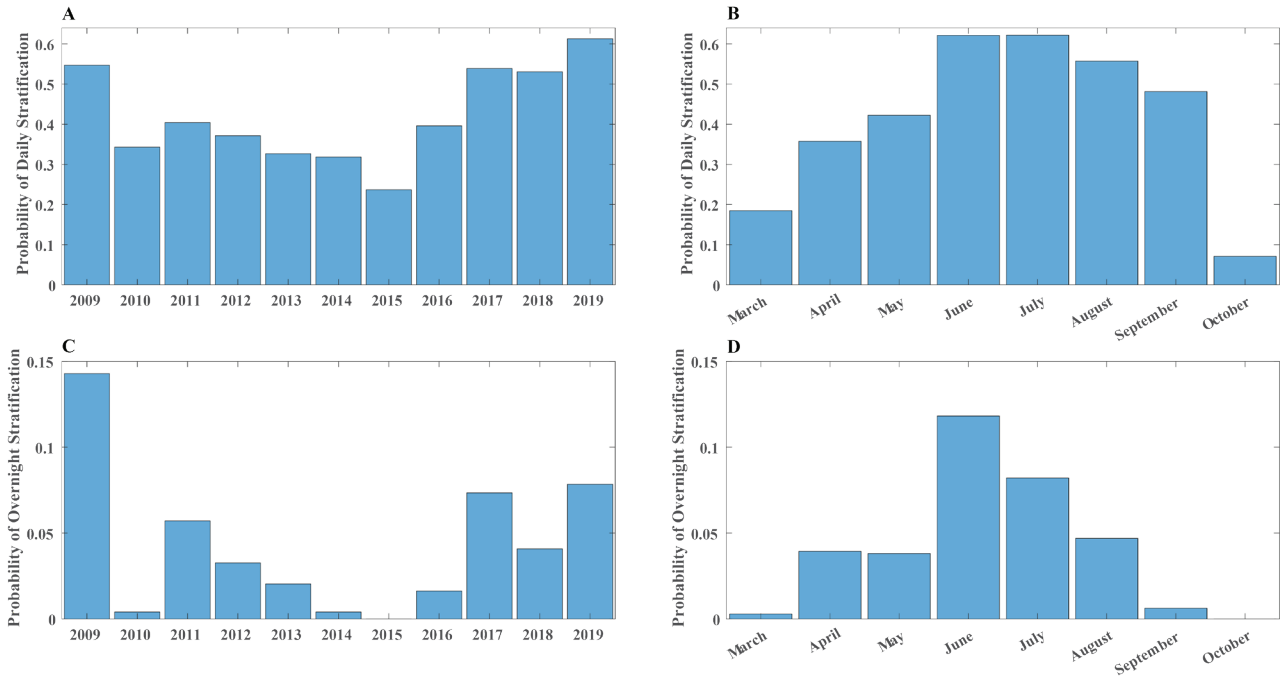

Figure 13 Probability of daily stratification on a (**A**) yearly basis and (**B**) monthly basis, and probability of overnight stratification on a (**C**) yearly basis and (**D**) monthly basis

of 78 W m^{-2}, on average, compared to heat flux ($\dot{Q}_{73}$) calculated with water temperature at CM73. Therefore, $\dot{Q}_{54}$ was adjusted with a regression: $\dot{Q}_{54} = 1.027 * \dot{Q}_{73} - 79.08$ ($R^2 = 0.99$, RMSE = 25.4 W m^{-2}).

The modeled potential energy anomaly from the long-term record (Φ_L) closely matched the modeled Φ_M during our study period (Figure 12). To accurately match the peaks in stratification between Φ_L and Φ_M during periods of low wind (i.e., mid-August), ε had to be increased from 0.0111 to 0.0185, likely as a result of differences in the input parameters (water velocity and heat flux) compared with the original model. Longer periods of stratification accumulate errors even with small discrepancies in the input parameters, because the modeled potential energy anomaly is computed by integrating over the entire period of stratification. Φ_L is also well correlated with Φ_C from the CTD casts ($R^2 = 0.83$, RMSE = 0.50) and Φ from the instrument string ($R^2 = 0.71$, RMSE = 0.89). On average, the difference in the duration of stratification between Φ_L and Φ was 0.003 hr (SD = 2.24 hr). We expect the long-term model to predict the general trends of stratification but expect some amount of uncertainty in the period of record outside of our study as a result of the adjustments in input parameters, tuning of ε, and lack of validation data.

Nevertheless, Φ_L was computed over the duration of the 11-year record, and we analyzed the yearly and monthly trends for the probability of daily and overnight stratification. We analyzed the period from March 1 to November 1 each year because the probability of stratification in other months was negligible. We defined daily stratification as daily integrated Φ_L exceeding 1 J m^{-3}, because this condition corresponded to periods of noticeable stratification (Figure 8B). We defined overnight stratification as stratification above 1 J m^{-3} that occurred through the night into the next day for at least 24 hr, since persistent stratification may be important in maintaining phytoplankton concentrations in the upper water column that can enhance production the next day (Cloern 1987).

https://doi.org/10.15447/sfews.2021v19iss4art5

The probability of March through November daily stratification varied on a yearly basis, with 2015 having the lowest probability and 2019 having the highest probability (Figure 13A). The probability of overnight stratification followed similar interannual patterns, with overnight stratification occurring most often in 2009 (Figure 13C). Averaging among years, we expect daily stratification on 102 days (41.6% of the time between March 1 and November 1) and 11 occurrences of overnight stratification (4.5% of the time), although recent years (2017–2019) have been above average. The interannual variability might be the result of longer time-scale climate fluctuations, which would require a record longer than 11 years to capture the variability in these relationships. The probability of stratification also varied on a monthly basis. In general, March and October had the fewest occurrences of daily and overnight stratification, while both stratification metrics were more frequent in June and July (Figure 13B and 13D). Variable patterns between the daily and overnight stratification on a yearly (Figure 13A and 13C) and monthly (Figure 13B and 13D) basis are likely because daily stratification depends primarily on the heat flux (a sufficiently hot day), while longer periods of stratification require persistent low wind speed to sustain overnight stratification for multiple days.

The monthly variability in daily integrated Φ_L magnitude was influenced by heat flux and wind, while water velocity was consistent from month to month (Figure 14), as expected. Thus, seasonal changes in potential energy anomaly were a function of heat flux and wind. The magnitude of daily integrated Φ_L also followed the daily stratification frequency by month. Overall, the month of June had the highest frequency of stratification (daily and overnight) and the highest potential energy magnitude based on the 11-year data set, which we attribute to the slightly higher level of heat flux and lower wind speed compared to other months, because stratification in our study area is at a delicate balance between these competing mechanisms.

DISCUSSION

Mixing Time-Scales and Mechanisms

The results of our study provide a detailed understanding of hydrodynamic processes in the upper DWSC, where tidal currents and wind together control mixing and stratification dynamics. Wind is important in increasing the occurrence of complete vertical mixing of the water column after the water column stratifies, and therefore can enhance transport by increasing shear at the surface and as a result of mixing from wind-wave action in the shallow and open water areas of the Delta (Lucas et al. 2006; Jones et al. 2008) and on the shallow benches within the DWSC (Morgan-King and Schoellhamer 2013). In our study, periods of sustained high winds increased vertical mixing, which increased dispersion, and therefore decreased both the longitudinal and vertical mixing time-scales. Considering tidal currents alone, longitudinal dispersion would be expected to be highest on flood tides as a result of stronger currents and an increase in shear in the water column; however, longitudinal dispersion was highest on windy ebbs as a result of increased shear near the surface. While the tidal currents are generally weak enough to allow stratification daily at our study site, the presence or absence of wind controls the duration of thermal stratification, especially stratification that continues overnight. In the absence of wind, the strongest stratification would be expected during neap tides when tidal current magnitudes are lowest; however, the longest period of stratification occurred from August 13 through 16 during a spring tide. Very weak wind speeds during this period did not provide the energy necessary to break down stratification, and the heat flux was sufficient to sustain stratification even under the stronger spring tide currents. However, stratification is unlikely in the southern end of the DWSC because the tidal currents are ~2.75 times higher than in our northern study area, making the effect of tidal currents $(2.75)^3$ or ~20 times higher in the energy balance. Tidal currents in our study area in the upper DWSC are sufficiently muted to allow periodic stratification events to last multiple days.

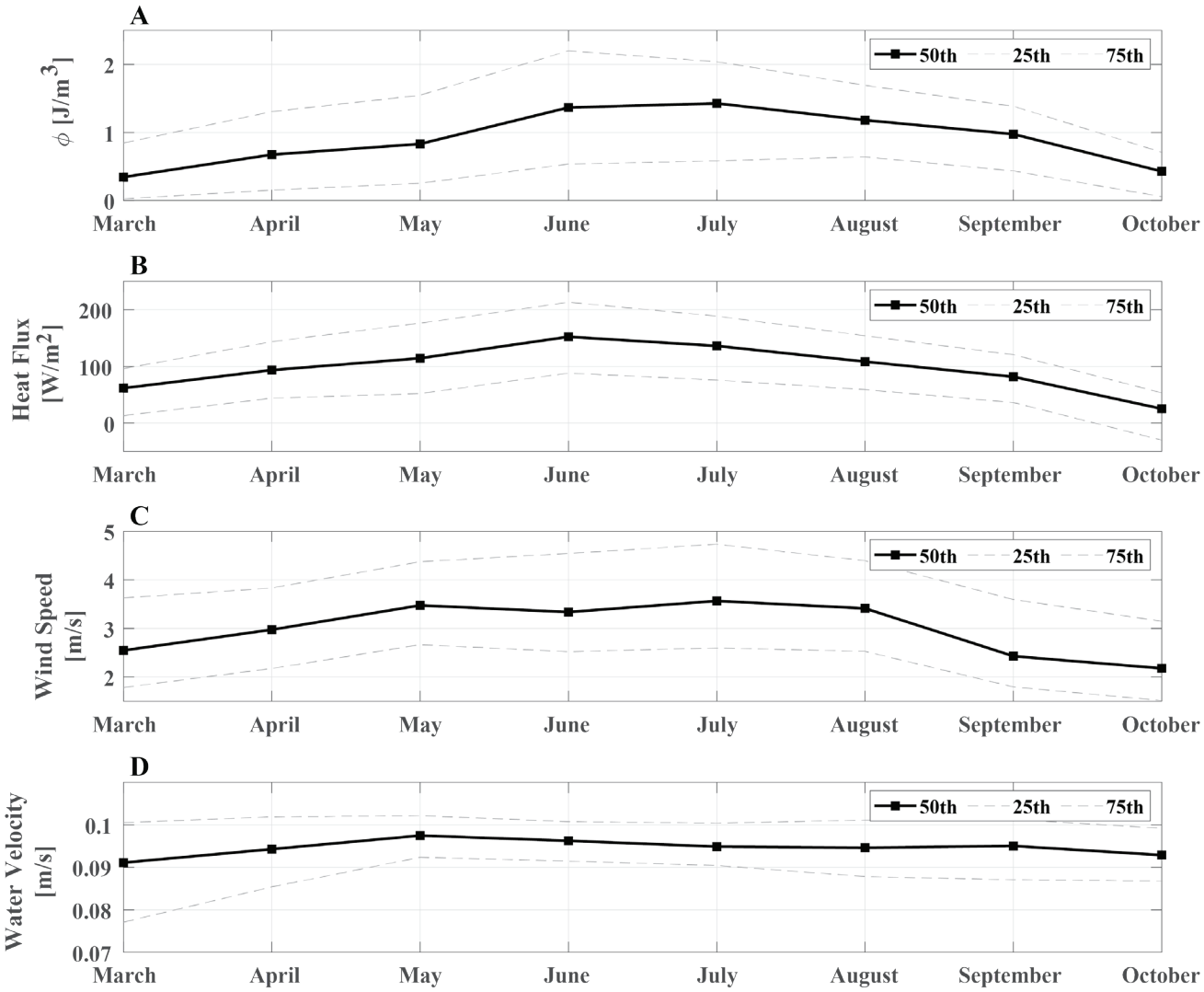

Figure 14 Monthly daily integrated median (50th; *black*), 25th and 75th (*dashed gray*) percentiles in (**A**) potential energy anomaly, (**B**) heat flux, (**C**) wind speed, and (**D**) water velocity from the 11-year energy balance calculation.

Our study supported a nutrient-addition experiment designed to assess whether phytoplankton production could be increased within the DWSC (USBR 2018). We examined the mixing time-scales to better understand the biological implications of stratification and mixing from wind, assuming sustained increases in phytoplankton biomass can occur when nutrients are not limiting and phytoplankton growth exceeds consumption and mixing time-scales (Lucas et al. 2009). The median time-scale for complete vertical mixing (1.1 hr) was shorter than either longitudinal (8.4 hr) or lateral (34.4 hr) mixing time-scales. In relation to diel patterns in chlorophyll-*a* (Figure 8C), the time-scales indicate that vertical and horizontal mixing is an important limitation on phytoplankton growth. Because mixing in the vertical dimension was consistently the fastest, and because it influences phytoplankton access to light and isolation from benthic grazers, stratification may be an important driver of the growth and accumulation of phytoplankton.

A stratified water column can isolate phytoplankton in the upper surface layer, providing enhanced light exposure in the photic zone, isolation from benthic grazers (Cloern

https://doi.org/10.15447/sfews.2021v19iss4art5

1991; Koseff et al. 1993), and reduced vertical dispersion. Studies throughout the estuary and Delta have observed increases in phytoplankton during stratification events (Cloern 1996; Lucas et al. 2016). While stratification developed most days during our study and is expected about 50% of summer days considering the long-term record, periods of sub-daily stratification appear to be too short to initiate a prolonged phytoplankton bloom (Lucas et al. 1998, 2016). During unstratified conditions, vertical mixing occurs on the order of 1 to 2 hr, and daily increases in chlorophyll-*a* rarely exceeded $3\,\mu g\,L^{-1}$, implying a net doubling growth rate of less than 1 day^{-1}. Interestingly, during stratification, the time-scale of vertical mixing slows to ~11 hr—the average duration of stratification—and the chlorophyll-*a* in the photic zone increased upwards of $13\,\mu g\,L^{-1}$ within a day (Figure 8C). This increase implies a faster growth rate when scaled only to the photic-zone growth rate (~1 to 2 day^{-1}), which allows phytoplankton to double or triple in concentration over the day. Thus, vertical dispersion may limit phytoplankton growth, which is temporarily lifted during stratification. These temporary blooms rarely persist overnight, because multi-day stratification events were infrequent during our study and over the long-term record. The persistence of overnight stratification may lead to increased productivity on the subsequent day if phytoplankton continue to remain isolated in the photic zone (Cloern 1987) and increased nutrient demands are satisfied. In this system—in addition to nutrients, light, and top-down grazing—stratification should be considered an important control on phytoplankton production.

Habitat Connectivity Along the DWSC

Connectivity between the DWSC and downstream channels, as well as exchange along the DWSC, is a function of both transport (advection by the tides) and mixing (dispersion). Spatial heterogeneity in transport and mixing along the DWSC determines how different habitats are formed along the channel, and ultimately the connectivity between these habitats, including the opportunity to provide subsidies from resource-abundant to resource-limited habitats (Cloern 2007).

Changes in both the tidal asymmetry and tidal current magnitude along the axis of the DWSC change the magnitude of advection and dispersion along the channel. Tidal wave propagation in most Delta channels is progressive in character, where stage and velocity are nearly in phase, and the magnitude of tidal currents on flood and ebb is similar. However, the DWSC is a terminal channel; therefore, the tidal wave changes from progressive to standing (where stage and velocity are out of phase), creating an increasingly flood-dominant tidal asymmetry along the axis of the channel. While the magnitude of tidal currents decreases moving landward in the DWSC—leading one to assume that both advection and mixing would similarly decrease—this is complicated by the tidal asymmetry, which becomes more pronounced in the upper DWSC. The tidal asymmetry associated with the standing wave character in the DWSC creates a flood tide bias that can increase net Lagrangian advection landward, the so-called Stokes Drift (Monismith 2020), even when the Eulerian net flows are zero. The influence of tidal asymmetry on dispersion is more difficult to determine because the tidal currents are not the only mechanism that contribute to dispersion.

The presence and timing of the wind also plays an important role in dispersion, increasing it over what would be predicted by tidal currents alone. For example, tracer-based longitudinal dispersion estimates averaged $17.4\,m^2\,s^{-1}$, with a range from 12 to $30\,m^2\,s^{-1}$, and were within range of other tracer-based estimates of dispersion in the Delta: 10 to $100\,m^2\,s^{-1}$ (Bailey 1966) and $32.7 \pm 3.6\,m^2\,s^{-1}$ (Schmieder et al. 2008). ADCP-based estimates were similar, at $20.0\,m^2\,s^{-1}$ on average, but had a larger range (5 to $125\,m^2\,s^{-1}$), likely because they were instantaneous estimates. Dispersion from oscillating tidal currents was $5.2\,m^2\,s^{-1}$ on average, similar to what is predicted by tidal currents in other parts of the Delta ($< 10\,m^2\,s^{-1}$; Sridharan et al. 2018). On average, tracer-based and ADCP-based estimates of longitudinal dispersion were 3 to 4 times greater than what would be predicted by tidal currents alone. We have observed that windy conditions on the ebb created the highest dispersion estimates in our

study area because the wind and currents act in opposing directions, which increased vertical shear.

The spatial heterogeneity in transport and mixing, described above, differentiates the pelagic zone along the length of the DWSC into different habitats. To first order, pelagic habitats in terminal channel systems like the DWSC differ based on their location relative to the tidal excursion length from the mouth of the channel, which also corresponds well with differences in water residence time, and can be defined as high-, low-, and no-exchange zones along the channel with respect to exchange with downstream habitats (Stumpner et al. 2020). Young et al. (2021) further showed that variability in pelagic habitats along the DWSC corresponds to changes in tidal forcing and exchange along the length of the channel, which influences turbidity, nutrient availability, primary and secondary production, and the abundance of pelagic organisms. For example, elevated zooplankton and phytoplankton concentrations have been measured in the no-exchange zone landward of our study area compared to elsewhere along the DWSC (Young et al. 2021), while the highest abundance of pelagic organisms—specifically shrimp and pelagic fishes—was observed seaward of our study area in the low-exchange zone (Feyrer et al. 2017; Young et al. 2021), where elevated turbidity may limit phytoplankton growth, suggesting a detrital food web (Young et al. 2021). We anticipate that dispersion rates are higher and stratification less likely in the low- and high-exchange zones of the DWSC seaward of our study area, given that tidal currents increase by a factor of ~2.75 from our study area to the mouth of the DWSC. Increases in dispersion and decreases in the mixing time-scales are expected to be an order of magnitude greater in the DWSC's low- and high-exchange zones because dispersion scales by the square of the velocity. Along the DWSC longitudinal axis, the decrease in tidally driven dispersion leads to a compression of habitats moving landward toward the channel terminus. Reduced mixing among adjacent water parcels and the associated increase in habitat isolation may lead to spatial heterogeneity in a number of ecologically important properties.

CONCLUSION

While tidal currents typically dominate the hydrodynamics in estuaries in general and in the San Francisco Estuary in particular, our detailed analysis of hydrodynamics revealed they are less dominant in the upper portion of the DWSC, a terminal channel where tidal currents are muted. Some of the relatively weaker physical processes that typically have little influence on transport elsewhere in the Delta—such as thermal stratification and its interaction with wind— can control mixing dynamics in the upper DWSC. Wind was a key mechanism in both breaking down stratification and increasing dispersion in our study, providing a source of variability that changed the mixing dynamics from a purely tidal current-driven system. Longitudinal dispersion rates were comparable to other studies in the Delta and were enhanced during periods of high wind. Wind mixing drove the breakdown of thermal stratification, but the development and strength of stratification was also influenced by the alignment of the tidal current phase with the heat flux and wind.

Transport and mixing in the upper DWSC will be altered by climatological changes in the system, specifically those that alter thermal stratification dynamics. Summers in the California Central Valley are characterized by warm, dry days and breezy, cool nights. However, with climate change, the Delta is experiencing both higher daytime and nighttime temperatures, with more frequent humid, nighttime heat waves (Mera et al. 2015; Gershunov and Guirguis 2012). Average summer wind speeds in the north Delta have decreased significantly in recent decades (Bever et al. 2018), reducing the cooling associated with the Delta breeze, which readily breaks down stratification in the DWSC most days in the summer. Summer conditions once commonplace in the Delta—breezy evenings and cool nights—are becoming less common (Mera et al. 2015; Bever et al. 2018) and may support stronger, more frequent, and longer-duration stratification

https://doi.org/10.15447/sfews.2021v19iss4art5

episodes in the DWSC. The balance between the magnitude of the physical processes that control stratification (wind, heat flux, and tidal currents), as well as the alignment of these processes (diurnal, semidiurnal, biweekly, and seasonally), could have a large influence on phytoplankton production in the DWSC in the future, as has been observed in other areas of the Delta (Lucas et al. 2006).

Management actions to encourage greater primary production in the DWSC are under consideration that would reconnect the DWSC to the Sacramento River and provide opportunity for riparian and channel margin habitat restoration (USBR 2018, 2019; Thomas et al. 2020). These proposed actions could take into account the physical processes for a given landscape, tidal, and meteorological forcing that limit thermal stratification, and consequently primary production, in order to improve management outcomes. For example, management actions that maintain or increase the presence of thermal stratification in the upper DWSC could effectively lengthen the vertical mixing time-scale to more consistently exceed phytoplankton growth time-scales. Given that time-scales of mixing and dispersion at our study site were likely shorter or very near the time-scales of phytoplankton growth, any increase in dispersion (i.e., faster mixing time-scales) or slowing of phytoplankton growth rates from higher current speeds and higher turbidity within the DWSC seaward of our study area may make it difficult to sustain phytoplankton growth as phytoplankton biomass is transported down the channel. Nevertheless, water inputs from the Sacramento River through the gates at the terminus of the DWSC could provide nitrogen to the upper DWSC when and where it is limiting, which could also support phytoplankton productivity. Restoration of tidal marsh habitat along the banks of the DWSC could increase the differences in tidal current magnitude between spring and neap tides, thereby increasing the range of longitudinal dispersion, exchanges between the DWSC and Cache Slough, and the physical footprint of the turbidity and associated biological maxima in the DWSC (Feyrer et al. 2017). Restoring hydrologic connectivity with the Sacramento River would introduce a net flow to the DWSC, likely altering the tidal asymmetry (depending on how it is operated), increasing tidal current magnitude, and increasing the rate of longitudinal dispersion, as was found by Monismith et al. (2009) in a similar setting. Further research and modeling is needed to determine the magnitude and extent of the potential operational changes on the existing mixing and stratification dynamics discussed in this paper. For example, introducing a low-to-modest net flow may not hinder the formation of stratification, since tidal currents were less important than wind speed in breaking down stratification. Additionally, we expect that increasing the connectivity of the DWSC with the Sacramento River, and allowing periodic higher flows, would increase the longitudinal dispersion rates and the connectivity of the various habitats within the DWSC, providing the potential to transport phytoplankton seaward in the DWSC when the mechanisms to support phytoplankton production are appropriately aligned. More modeling could be done to determine the level of phytoplankton production that could be reached in the DWSC, and to investigate the effect and timing of intermittent net flows on export from the DWSC.

The characteristics of the DWSC that support increased phytoplankton production in the summer—a terminal channel with long residence times and episodic thermal stratification—could be used understand the interactions between the primary physical forcing mechanisms at play and inform habitat restoration efforts elsewhere in the Delta. Finally, the energy balance analysis may be valuable in evaluating proposed changes to landscapes based on their ability to concurrently allow for longer residence times (dendritic channel systems, less flow-through/conveyance channels) and greater frequency of occurrence and duration of thermal stratification as a means of increasing phytoplankton production in the Delta.

ACKNOWLEDGMENTS

We thank Erwin Van Nieuwenhuyse for his invaluable contributions to the manuscript and the US Bureau of Reclamation for providing funding for the project. Thank you to Lisa Lucas of the USGS for her thorough review, which greatly improved the manuscript, and to two anonymous reviewers for their thoughtful comments on this manuscript. Thank you to Cathy Ruhl, Norbert Vandenbranden, Trevor Violette, Mark Inc, Brittany Griffiths, Chany Huddleston Adrianza, Henry Rabas, Zach Houseworth, Anna Conlen, Ryan Johnson, Chris Vallee, Norman Soeder, Joe Hatfield, Tosha Duncan, Mike Porter, and Brian Bergamaschi of the USGS California Water Science Center for their assistance with instrumentation, field work, and technical support.

DISCLAIMER

Any use of trade, firm, or product names is for descriptive purposes only and does not imply endorsement by the US Government.

REFERENCES

Abarbanel H, Holm D, Marsden J, Ratiu T. 1984. Richardson number criterion for the nonlinear stability of three-dimensional stratified flow. Phys Rev Lett. [accessed 2021 Oct 7];52:2352-2355. *https://doi.org/10.1103/PhysRevLett.52.2352*

Bailey TE. 1966. Fluorescent-tracer ttudies of an estuary. J Water Pollut Control Federation. [accessed 2021 Oct 7];38(12):1986-2001. Available from: *https://www.jstor.org/stable/25035696*

Bever AJ, MacWilliams ML, Fullerton DK. 2018. Influence of an observed decadal decline in wind speed on turbidity in the San Francisco Estuary. Estuaries Coasts. [accessed 2021 Oct 7];41:1943-1967. *https://doi.org/10.1007/s12237-018-0403-x*

Burchard H, Hofmeister R. 2008. A dynamic equation for the potential energy anomaly for analysing mixing and stratification in estuaries and coastal seas. Estuar Coast Shelf Sci. [accessed 2021 Oct 7];77(4):679-687. *https://doi.org/10.1016/j.ecss.2007.10.025*

Carr ML, Rehmann CR. 2007. Measuring the dispersion coefficient with acoustic Doppler current profilers. J Hydraul Eng. [accessed 2021 Oct 7];133(8):977-982. *https://doi.org/10.1061/(ASCE)0733-9429(2007)133:8(977)*

[CDFW]. California Department of Fish and Wildlife 2019. State and federally listed endangered and threatened animals of California. Updated October 2021. [accessed 2021 Oct 7]. Available from: *https://nrm.dfg.ca.gov/FileHandler.ashx?DocumentID=109405&inline*

Cloern JE. 1987. Turbidity as a control on phytoplankton biomass and productivity in estuaries. Cont Shelf Res. [accessed 2021 Oct 7];7(11-12):1367-1381. *https://doi.org/10.1016/0278-4343(87)90042-2*

Cloern JE. 1991. Annual variations in river flow and primary production in the south San Francisco Bay estuary. In: Elliot M, Ducrotoy JP, editors. Estuaries and coasts: spatial and temporal intercomparisons. Denmark: Olsen and Olsen Publishers. p. 91-96.

Cloern JE. 1996. Phytoplankton bloom dynamics in coastal ecosystems: a review with some general lessons from sustained investigation of San Francisco Bay, California. Rev Geophys. [accessed 2021 Oct 7];34(2):127-168. *https://doi.org/10.1029/96RG00986*

Cloern JE. 2001. Our evolving conceptual model of the coastal eutrophication problem. Mar Ecol Prog Ser. [accessed 2021 Oct 7];210:223-253. *https://doi.org/10.3354/meps210223*

Cloern JE; Grover JP, associate editor; DeAngelis DL, editor. 2007. Habitat connectivity and ecosystem productivity: implications from a simple model. Am Nat. [accessed 2021 Oct 7];169(1):E21-33. *https://www.doi.org/10.1086/510258*

Cloern JE, Foster SQ, Kleckner AE. 2014. Phytoplankton primary production in the world's estuarine-coastal ecosystems. Biogeosciences. [accessed 2021 Oct 7];11:2477-2501. *https://doi.org/10.5194/bg-11-2477-2014*

Crawford JT, Loken LC, Casson NJ, Smith C, Stone AG, Winslow LA. 2015. High-speed limnology: using advanced sensors to investigate spatial variability in biogeochemistry and hydrology. Environ Sci Technol. [accessed 2021 Oct 7];49(1):442-450. *https://doi.org/10.1021/es504773x*

Downing BD, Bergamaschi BA, Kendall C, Kraus TEC, Dennis KJ, Carter JA, Von Dessonneck TS. 2016. Using continuous underway isotope measurements to map water residence time in hydrodynamically complex tidal environments. Environ Sci Technol. [accessed 2021 Oct 7];50(24):13387-13396. *https://doi.org/10.1021/acs.est.6b05745*

Dronkers J. 1986. Tidal asymmetry and estuarine morphology. Neth J Sea Res. [accessed 2021 Oct 7];20(2-3):117-131. *https://doi.org/10.1016/0077-7579(86)90036-0*

Fischer HB, List EJ, Koh RCY, Imberger J, Brooks NH. 1979. Mixing in inland and coastal waters. New York (NY): Academic Press, Inc.

Feyrer F, Slater SB, Portz DE, Odom D, Morgan-King T, Brown LR. 2017. Pelagic nekton abundance and distribution in the northern Sacramento–San Joaquin Delta, California. Trans Am Fish Soc. [accessed 2021 Oct 7];146(1):128-135. *https://doi.org/10.1080/00028487.2016.1243577*

Frenzel CW. 1962. Diurnal wind variations in central California. J Appl Meteorol. [accessed 2021 Oct 7];1(3):405–412. *https://doi.org/10.1175/1520-0450(1962)001<0405:DWVICC>2.0.CO;2*

Galperin B, Sukoriansky S, Anderson PS. 2007. On the critical Richardson number in stably stratified turbulence. Atmos Sci Lett. [accessed 2021 Oct 7];8(3):65-69. *https://doi.org/10.1002/asl.153*

Gershunov A, Guirguis K. 2012. California heat waves in the present and future. Geophys Res Lett. [accessed 2021 Oct 7];39(18). *https://doi.org/10.1029/2012GL052979*

Geyer WR, Chant R, Houghton R. 2008. Tidal and spring-neap variations in horizontal dispersion in a partially mixed estuary. J Geophys Res–Oceans [accessed 2021 Oct 7];113(C7). *https://doi.org/10.1029/2007JC004644*

Geyer WR, Ralston DK. 2011. The dynamics of strongly stratified estuaries. Chapter 2.03 in: Wolanski E, McLusky DS, editors. Treatise on estuarine and coastal science. Vol. 2. [accessed 2021 Oct 7]. Waltham (MA): Academic Press. p. 37-51. Available from: *https://www.otago.ac.nz/marinescience/MARI401/MARI401_2013/MARI401%20Doubtful%20References/geyer&%20ralton%20stronly%20stratified%20estuarys.pdf*

Gill A. 1982. Atmosphere-ocean dynamics. London (United Kingdom): Academic Press. 662 p.

Godin G. 1972. The analysis of tides. Toronto (Canada): University of Toronto Press.

Hoitink AJF, Jay DA. 2016. Tidal river dynamics: implications for deltas. Rev Geophys. [accessed 2021 Oct 7];54(1):240-272. *https://doi.org/10.1002/2015RG000507*

Howard L. 1961. Note on a paper of John W. Miles. J Fluid Mech. [accessed 2021 Oct 7];10:509–512. *https://doi.org/10.1017/S0022112061000317*

Jones NL, Thompson JK, Monismith SG. 2008. A note on the effect of wind waves on vertical mixing in Franks Tract, Sacramento-San Joaquin Delta, California. San Franc Estuary Watershed Sci. [accessed 2021 Oct 7];6(2). *https://doi.org/10.15447/sfews.2008v6iss2art4*

Koseff JR, Holen JK, Monismith SG, Cloern JE. 1993. Coupled effects of vertical mixing and benthic grazing on phytoplankton populations in shallow turbid estuaries. J Mar Res. [accessed 2021 Oct 7];51(4):843-868. *https://doi.org/10.1357/0022240933223954*

Lenoch LEK, Loken LC, Stumpner PR, Sadro S, Van Nieuwenhuyse EE, Burau JR, Dahlgren RA, Beaver J. 2021. Nutrient addition experiment in the Sacramento River Deep Water Ship Channel: US Geological Survey data release. [accessed 2021 Oct 7]. *https://doi.org/10.5066/P9SKCIUW*

Lettau HH. 1979. Wind and temperature profile prediction for diabatic surface layers including strong inversion cases. Bound-Layer Meteorol. [accessed 2021 Oct 7];17:443–464. *https://doi.org/10.1007/BF00118610*

Levesque VA, Oberg KA. 2012. Computing discharge using the index velocity method: techniques and methods 3–A23.Reston (VA): US Geological Survey. [accessed 2021 Oct 7]. 148 p. *https://doi.org/10.3133/tm3A23*

Loken LC, Van Nieuwenhuyse EE, Dahlgren RA, Lenoch LEK, Stumpner PR, Burau JR, Sadro S. 2021. Assessment of multiple ecosystem metabolism methods in an estuary. Limnol Oceanogr: Methods. [accessed 2021 Oct 7]. *http://doi.org/10.1002/lom3.10458*

Lucas LV, Cloern JE, Koseff JR, Monismith SG, Thompson JK. 1998. Does the Sverdrup critical depth model explain bloom dynamics in estuaries? J Mar Res. [accessed 2021 Oct 7];56(2):375–415. *https://doi.org/10.1357/002224098321822357*

Lucas LV, Sereno DM, Burau JR, Schraga TS, Lopez CB, Stacey MT, Parchevsky KV, Parchevsky VP. 2006. Intradaily variability of water quality in a shallow tidal lagoon: mechanisms and implications. Estuaries Coasts. [accessed 2021 Oct 7];29(5):711-730. *https://doi.org/10.1007/BF02786523*

Lucas LV, Thompson JK, Brown LR. 2009. Why are diverse relationships observed between phytoplankton biomass and transport time? Limnol Oceanogr. [accessed 2021 Oct 7];54(1):381-390. *https://doi.org/10.4319/lo.2009.54.1.0381*

Lucas LV, Cloern JE, Thompson JK, Stacey MT, Koseff JR. 2016. Bivalve grazing can shape phytoplankton communities. Front Mar Sci. [accessed 2021 Oct 7];3:14. *https://doi.org/10.3389/fmars.2016.00014*

Mera R, Massey N, Rupp DE, Mote P, Allen M, Frumhoff PC. 2015. Climate change, climate justice and the application of probabilistic event attribution to summer heat extremes in the California Central Valley. Clim Change. [accessed 2021 Oct 7];133:427-438. *https://doi.org/10.1007/s10584-015-1474-3*

Miles J. 1961. On the stability of heterogeneous shear flows. J Fluid Mech. [accessed 2021 Oct 7];10(4):496–508. *https://doi.org/10.1017/S0022112061000305*

Monin AS, Yaglom AM. 1972. Statistical fluid mechanics: mechanics of turbulence. Vol. I. Cambridge (MA): The MIT Press.

Monismith SG, Burau JR, Stacey MT. 1996. Stratification dynamics and gravitational circulation in northern San Francisco Bay. In: Hollibaugh JT, editor. San Francisco Bay: the ecosystem. Proceedings of the 75th Annual Meeting of the Pacific Division of the American Association for the Advancement of Science; 1994 June 19-24; San Francisco (CA): AAAS, Pacific Division. p. 123-153.

Monismith SG, Hench JL, Fong DA, Nidzieko NJ, Fleenor WE, Doyle LP, Schladow SG. 2009. Thermal variability in a tidal river. Estuaries Coasts. [accessed 2021 Oct 7];32:100-110. *https://doi.org/10.1007/s12237-008-9109-9*

Monismith SG. 2020. Stokes drift: theory and experiments. J Fluid Mech. [accessed 2021 Oct 7];884:F1. *https://doi.org/10.1017/jfm.2019.891*

Morgan-King TL, Schoellhamer DH. 2013. Suspended-sediment flux and retention in a backwater tidal slough complex near the landward boundary of an estuary. Estuaries Coasts. [accessed 2021 Oct 7];36:300-318. *https://doi.org/10.1007/s12237-012-9574-z*

Moyle PB, Brown LR, Durand JR, Hobbs JA. 2016. Delta Smelt: life history and decline of a once-abundant species in the San Francisco Estuary. San Franc Estuary Watershed Sci. [accessed 2021 Oct 7];14(2). *https://doi.org/10.15447/sfews.2016v14iss2art6*

Parsons DR, Jackson PR, Czuba JA, Engel FL, Rhoads BL, Oberg KA, Best JL, Mueller DS, Johnson KK, Riley JD. 2013. Velocity Mapping Toolbox (VMT): a processing and visualization suite for moving-vessel ADCP measurements. Earth Surf Process Landf. [accessed 2021 Oct 7];38(11):1244-1260. *https://doi.org/10.1002/esp.3367*

Pawlowicz R, Beardlsey B, Lentz S, Dever E, Anis A. 2001. Software simplifies air–sea data estimates. EOS Trans AGU. [accessed 2021 Oct 7];82(1):1-6. *https://doi.org/10.1029/01EO00004*

R Core Team. 2020. R: a language and environment for statistical computing. Vienna (Austria): R Foundation for Statistical Computing, [accessed 2021 Oct 7]. Available from: *https://www.R-project.org*

Robinson A, Richey A, Cloern JE, Boyer KE, Burau J, Canuel E, DeGeorge J, Drexler JZ, Howe ER, Kneib R, et al. 2016. Primary production in the Sacramento-San Joaquin Delta: a science strategy to quantify change and identify future potential. Richmond (CA): San Francisco Estuary Institute–Aquatic Science Center. Report of SFEI–ASC's Resilient Landscapes Program, Publication #781. [accessed 2021 Oct 7]. 95 p. Available from: *https://www.sfei.org/sites/default/files/biblio_files/Primary%20Production%20in%20the%20Sacramento-San%20Joaquin%20Delta%206-1-2016.pdf*

Ruhl CA, Simpson MR. 2005. Computation of discharge using the index velocity method in tidally affected areas. Sacramento (CA): US Geological Survey Scientific Investigations Report No. 2005-5004. [accessed 2021 Oct 7]. 41 p. *https://doi.org/10.3133/sir20055004*

Schladow SG, Monismith SG. 2009. Hydrodynamics and oxygen modeling of the Stockton Deep Water Ship Channel. Final report for CALFED ERP-02D-P51. [accessed 2021 Oct 7]. 274 p. Available from: *http://watershed.ucdavis.edu/pdf/Schladow-Monismith-2009.pdf*

Schmieder PJ, Ho DT, Schlosser P, Clark JF, Schladow SG. 2008. An SF6 tracer study of the flow dynamics in the Stockton Deep Water Ship Channel: implications for dissolved oxygen dynamics. Estuaries Coasts. [accessed 2021 Oct 7];31:1038-1051. *https://doi.org/10.1007/s12237-008-9093-0*

Shen C, Niu J, Anderson E.J, Phanikumar MS. 2010. Estimating longitudinal dispersion in rivers using Acoustic Doppler Current Profilers. Adv Water Resour. [accessed 2021 Oct 7];33(6):615-623. *https://doi.org/10.1016/j.advwatres.2010.02.008*

Simpson JH, Bowers G. 1981. Models of stratification and frontal movement in shelf seas. Deep Sea Res Part A. Oceanogr Res Pap. [accessed 2021 Oct 7];28(7):727-738. *https://doi.org/10.1016/0198-0149(81)90132-1*

Soetaert K, Petzoldt T. 2020. marelac: tools for aquatic sciences. R package version 2.1.10. [accessed 2021 Oct 7]. Available from: *https://CRAN.R-project.org/package=marelac*

Sommer T, Armor C, Baxter R, Breuer R, Brown L, Chotkowski M, Culberson S, Feyrer F, Gingras M, Herbold B, et al. 2007. The collapse of pelagic fishes in the upper San Francisco Estuary: El colapso de los peces pelagicos en la cabecera Del Estuario San Francisco. Fisheries. [accessed 2021 Oct 7];32(6):270-277. *https://doi.org/10.1577/1548-8446(2007)32[270:TCOPFI]2.0.CO;2*

Sommer T, Mejia F. 2013. A place to call home: a synthesis of Delta Smelt habitat in the upper San Francisco Estuary. San Franc Estuary Watershed Sci. [accessed 2021 Oct 7];11(2). *https://doi.org/10.15447/sfews.2013v11iss2art4*

SonTek. 2017. CastAway CTD: user's manual 1.5 (October 2017). San Diego (CA): Xylem. [accessed 2021 Oct 7]. Available from: *https://www.fondriest.com/pdf/ysi_castaway_manual.pdf*

Sridharan VK, Monismith SG, Fong DA, Hench JL. 2018. One-dimensional particle tracking with streamline preserving junctions for flows in channel metworks. J Hydraul Eng. [accessed 2021 Oct 7];144(2). *https://doi.org/10.1061/(ASCE)HY.1943-7900.0001399*

Stumpner PR, Burau JR, Forrest AL. 2020. A Lagrangian-to-Eulerian metric to identify estuarine pelagic habitats. Estuaries Coasts. [accessed 2021 Oct 7];44:1231-1249. *https://doi.org/10.1007/s12237-020-00861-7*

Thomas J, Malakpet C, Konieczki M, Cavallo B. 2020. Stone Lock water quality and ecosystem enhancement project: alternatives analysis technical memorandum. Sacramento (CA): Jacobs Engineering Group Inc. 81 p.

UNESCO. 1981. The practical salinity scale 1978 and the international equation of state of seawater 1980. UNESCO Technical papers in Marine Science 36. Tenth repors of the joint panel on oceanographic tables and standards. [accessed 2021 Oct 7]. 28 p. Sidney (BC): UNESCO. Available from: *https://www.jodc.go.jp/info/ioc_doc/UNESCO_tech/046148eb.pdf*

[USBR] US Bureau of Reclamation. 2018. Environmental assessment: Sacramento Deep Water Ship Channel nutrient enrichment project. Sacramento (CA): USBR, Midwest Pacific Region. [accessed 2021 Jun 08]. Available from: *https://www.usbr.gov/mp/nepa/includes/documentShow.php?Doc_ID=35182*

[USBR] US Bureau of Reclamation. 2019. Environmental assessment: Sacramento Deep Water Ship Channel nutrient enrichment project: phase 2. Sacramento (CA): USBR, Midwest Pacific Region. [accessed 2021 Nov 16]. Available from: *https://www.usbr.gov/mp/nepa/includes/documentShow.php?Doc_ID=39642*

[USGS] US Geological Survey. 2021. National Water Information System web interface. Water data for the nation. [accessed 2021 Nov 10]. *https://doi.org/10.5066/F7P55KJN*

Vroom J, van der Wegen M, Martyr-Koller RC, Lucas LV. 2017. What determines water temperature dynamics in the San Francisco Bay-Delta System? Water Resour Res. [accessed 2021 Oct 7];53(11):9901–9921. *https://doi.org/10.1002/2016WR020062*

Walters RA, Cheng RT, Conomos TJ. 1985. Time scales of circulation and mixing processes of San Francisco Bay waters. Hydrobiologia. [accessed 2021 Oct 7];129:13-36. *https://doi.org/10.1007/BF00048685*

Whipple AA, Grossinger RM, Rankin D, Stanford B, Askevold RA. 2012. Sacramento–San Joaquin Delta historical ecology investigation: exploring pattern and process. Prepared for the California Department of Fish and Game and Ecosystem Restoration Program. A report of SFEI-ASC's Historical Ecology Program, Publication #672. Richmond (CA): San Francisco Estuary Institute-Aquatic Science Center. [accessed 2021 Oct 7]. 438 p. Available from: *https://www.sfei.org/sites/default/files/biblio_files/Delta_HistoricalEcologyStudy_SFEI_ASC_2012_highres.pdf*

Woodroffe CD. 2002. Coasts: form, process, and evolution. Cambridge (UK): Cambridge University Press.

Wurtsbaugh WA, Paerl HW, Dodds WK. 2019. Nutrients, eutrophication and harmful algal blooms along the freshwater to marine continuum. WIREs Water. [accessed 2021 Oct 7]; 6(5):e1373. *https://doi.org/10.1002/wat2.1373*

Yamamoto G. 1975. Generalization of the KEYPS formula in diabatic conditions and related discussion on the critical Richardson number. J Meteorol Soc Japan. [accessed 2021 Oct 7];53(3):189–195. *https://doi.org/10.2151/jmsj1965.53.3_189*

Young M, Feyrer F, Stumpner P, Larwood V, Patton O, Brown L. 2021. Hydrodynamics drive pelagic communities and food web structure in a tidal environment. Int Rev Hydrobiol. [accessed 2021 Oct 7];106:69–85. *https://doi.org/10.1002/iroh.202002063*

Zaremba LL and Carroll JJ. 1999. Summer wind flow regimes over the Sacramento Valley. J Appl Meteorol. [accessed 2021 Oct 7];38:1463-1473. *https://doi.org/10.1175/1520-0450(1999)038<1463:SWFROT>2.0.CO;2*

https://doi.org/10.15447/sfews.2021v19iss4art5